



A rechargeable coating with temporal-sequence antibacterial activity and soft tissue sealing

Fang Wang^{a,b}, Shiwei Guan^{a,b}, Min Xing^c, Wenhao Qian^c, Jiajun Qiu^{a,**}, Xuanyong Liu^{a,b,d,*}

^a State Key Laboratory of High Performance Ceramics and Superfine Microstructure, Shanghai Institute of Ceramics, Chinese Academy of Sciences, Shanghai, 200050, PR China

^b Center of Materials Science and Optoelectronics Engineering, University of Chinese Academy of Sciences, Beijing, 100049, PR China

^c Shanghai Xuhui District Dental Center, Shanghai, 200032, PR China

^d State Key Laboratory for Modification of Chemical Fibers and Polymer Materials, College of Biological Science and Medical Engineering, Donghua University, Shanghai, 201620, PR China

ARTICLE INFO

Keywords:

Polyimides
Medical titanium
Transcutaneous implants
Antibacterial
Soft tissue sealing

ABSTRACT

Transcutaneous implants that penetrate through skin or mucosa are susceptible to bacteria invasion and lack proper soft tissue sealing. Traditional antibacterial strategies primarily focus on bacterial eradication, but excessive exposure to bactericidal agents can induce noticeable tissue damage. Herein, a rechargeable model (HPI-Ti) was constructed using perylene polyimide, an aqueous battery material, achieving temporal-sequence regulation of bacterial killing and soft tissue sealing. Charge storage within HPI-Ti is achieved after galvanostatic charge, and chemical discharge is initiated when immersed in physiological environments. During the early discharge stage, post-charging HPI-Ti demonstrates an antibacterial rate of $99.96 \pm 0.01\%$ for 24 h, preventing biofilm formation. Contact-dependent violent electron transfer between bacteria and the material causes bacteria death. In the later discharge stage, the attenuated discharging status creates a gentler electron-transfer micro-environment for fibroblast proliferation. After discharge, the antibacterial activity can be reinstated by recharge against potential reinfection. The antibacterial efficacy and soft tissue compatibility were verified *in vivo*. These results demonstrate the potential of the charge-transfer-based model in reconciling antibacterial efficacy with tissue compatibility.

1. Introduction

Transcutaneous and transmucosal implant-related infections have attracted wide attention. As transcutaneous implants, such as dental implants and external fixators, are increasingly utilized in medical treatments, bacterial infection at the soft tissue-implant interface poses a significant concern [1–3]. Transcutaneous implants penetrate through the intact skin or mucosa, leading to the exposure of the interior of the human body to foreign substances [4]. The gap between artificial materials and the skin or mucosa disrupts the skin's natural barrier against pathogenic factors [5]. Following the invasion, bacteria competitively adhere to the surface of biomaterials, hindering the sealing of soft tissues [6]. Moreover, the adverse effects of bacterial infections will rapidly exacerbate over time, and these versatile bacteria that adhere to

biomaterial surfaces aggregate in extracellular polymeric substances to form biofilms, which exhibit resistance to antibiotics and host defense [7]. Therefore, it is crucial to eliminate bacteria efficiently during the initial adhesion stage.

Biomedical titanium and its alloy are commonly used for transcutaneous implants due to their biocompatibility and good mechanical properties [8]. However, the absence of antibacterial activities on titanium surfaces represents a major drawback, which has been addressed through strategies such as incorporating antibiotic agents or antimicrobial peptides, as well as surface modification using inorganic antibacterial metal elements, graphene oxide derivatives, and antibacterial polymers [9–13]. A better soft tissue sealing can be a natural and potent barrier against bacteria [14,15]. However, achieving both optimal antibacterial efficacy and tissue regeneration proves challenging, giving

Peer review under responsibility of KeAi Communications Co., Ltd.

* Corresponding author.

** Corresponding author.

E-mail addresses: qiujiujun@mail.sic.ac.cn (J. Qiu), xyliu@mail.sic.ac.cn (X. Liu).

<https://doi.org/10.1016/j.bioactmat.2024.05.029>

Received 6 March 2024; Received in revised form 27 April 2024; Accepted 14 May 2024

2452-199X/© 2024 The Authors. Publishing services by Elsevier B.V. on behalf of KeAi Communications Co. Ltd. This is an open access article under the CC BY-NC-ND license (<http://creativecommons.org/licenses/by-nc-nd/4.0/>).

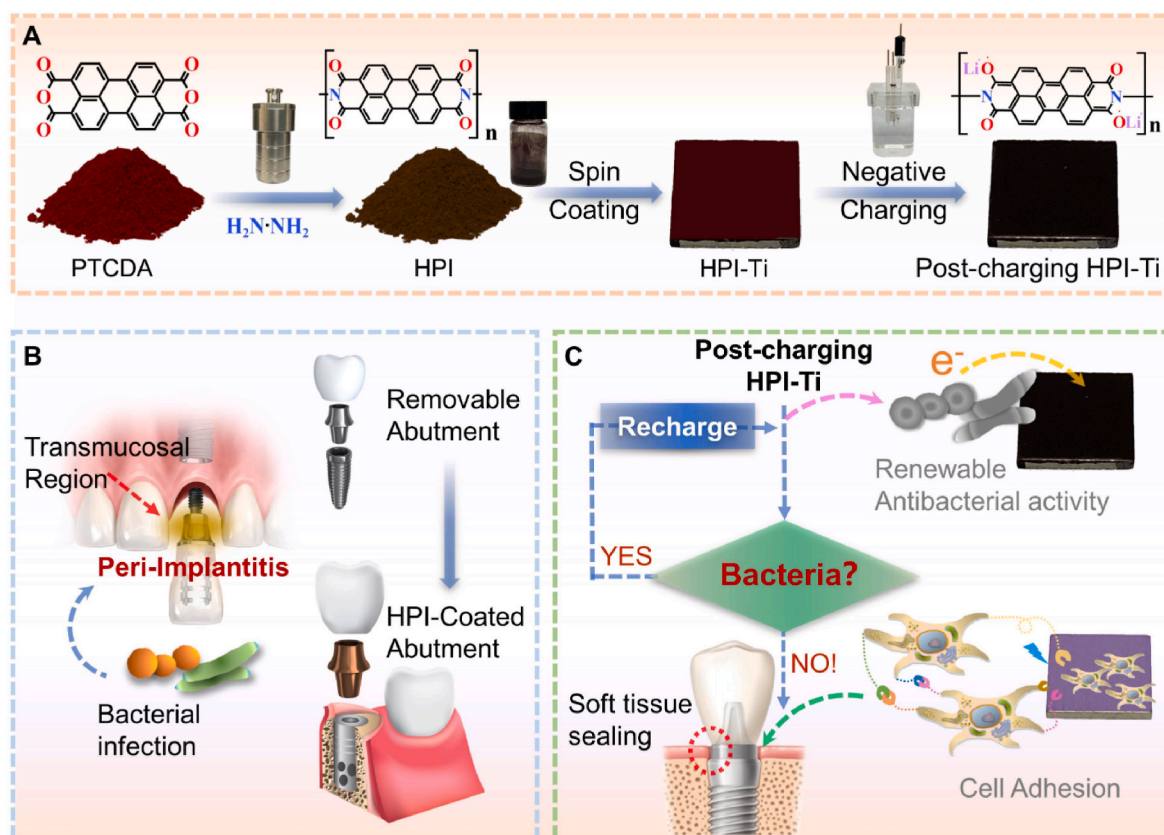
rise to a paradox. Excessive exposure to bactericidal agents that exhibit significant antibacterial properties has been found to induce noticeable tissue damage [16–18]. Therefore, to mitigate the cumulative impacts of prolonged exposure to antibacterial materials and provide a conducive environment for soft tissue repair, it is highly desirable to design temporal-sequence regulatable surfaces, which can kill bacteria while enhancing cell adhesion at the initial competitive adhesion stage, and then facilitating cell proliferation in the later tissue-repair stage.

A better understanding of metabolic activity in bacterial and mammalian cells may inspire the design of an efficient antibacterial strategy at the initial contact stage. Electron transport is a fundamental process for the vital functions of cells [19–22]. The concept of contact-dependent electron transfer between bacteria and materials has been previously proposed in the field of microbial fuel cells [23] and, more recently, in prospective antibacterial research [24–26]. Theoretical and experimental investigations have demonstrated that the introduction of surface charges can compromise the structural and functional integrity of bacterial membranes [27,28]. The implementation of a post-charging capacitive material capable of energy storage or charge accumulation proves to be a straightforward bactericidal strategy [29]. Additionally, electrical signals play an essential role in wound healing [30]. Specifically, an endogenous electrical field is generated around a wound following skin trauma, which elicits cell migration towards the central region of the wound and facilitates tissue sealing [31,32].

Perylene polyimides containing carbonyl groups represent typical organic electrode materials demonstrating excellent redox stability and high reversible capacities [33–35]. Polyimide material has been proposed for antitumor application due to its exceptional capacity and non-toxic nature [36]. Electron transfer is involved in conjugated aromatic polyimide during the charge and discharge process [37]. Modifying titanium surfaces with polyimide coating can be a viable strategy to induce surface electron transfer, achieving potent antibacterial

effects. The electron transfer in reversible keto-enol transformation of the polyimide during charge and discharge may result in renewable antibacterial effects. Different electron-transfer activities in early and later discharging stages can enable the temporal-sequence regulation.

In this study, hydrazine hydrate-derived polyimide (HPI) synthesized from perylene-3,4,9,10-tetracarboxylic dianhydride is coated on titanium (HPI-Ti) to design the temporal-sequence regulatable model described in Scheme 1A. HPI-Ti achieved reversible charge/discharge performances, enabling the charge, discharge, and recharge of the antibacterial model. The antibacterial efficacy of HPI-Ti is achieved through negative charging and can be repeatedly charged to restore its antimicrobial activity. As illustrated in Scheme 1B-C, this strategy can be applied to the removable abutment on titanium dental implants to fabricate an HPI-coated abutment with renewable antibacterial activity. After implantation, post-charging HPI-Ti can effectively kill bacteria through potent charge-transfer interaction during the early discharge stage while promoting cell adhesion and migration by influencing the expression of cell adhesion-related proteins. If bacterial infection occurs during use, the abutment can be removed for recharging and reinstallation to enhance antibacterial activity. If there is no more bacterial infection, the HPI-coated modified abutment can be retained and utilized to enhance soft tissue sealing by facilitating cell and tissue adhesion through the electrical signals generated by its charge transfer. During the later discharge stage, the attenuated discharge status can create a milder electron-transfer micro-environment for fibroblast proliferation. The antibacterial efficacy and soft tissue compatibility are investigated *in vivo* and *in vitro* to verify the model's effectiveness. The systematic study on the rechargeable HPI-Ti presents a tactic for designing temporal-sequence-regulated implanted devices with enhanced antibacterial efficacy and soft tissue compatibility.



Scheme 1. Schematic illustration of (A) synthesis processes for HPI, HPI-Ti, and post-charging HPI-Ti, along with (B–C) the application of rechargeable HPI-Ti for removable abutment on titanium dental implants.

2. Results and discussion

2.1. Preparation and characterization

The synthesis of HPI powder was initially conducted via the solvothermal method, with perylene-3,4,9,10-tetracarboxylic dianhydride (PTCDA) serving as the primary precursor material (Fig. 1A). The FTIR spectrum in Fig. 1B reveals that PTCDA exhibits two broad infrared vibration bands at 1771 and 1721 cm^{-1} , which correspond to the asymmetric and symmetric stretching vibrations of C=O bonds. The characteristic peaks of the HPI diminish in this spectral region, while new peaks emerge at approximately 1700 and 1660 cm^{-1} . The redshift of carbonyl characteristic peaks can be ascribed to spatial and resonance effects associated with polymerization reactions. Additionally, a peak at 1367 cm^{-1} from HPI can be attributed to the stretching vibration of C–N bonds within the polyimide ring. The polymerization of HPI through the imide region facilitates π -electron delocalization and preserves the integrity of carbonyl groups, which can function as redox centers in electrochemical charging/discharging [35]. The X-ray diffraction patterns of PTCDA and HPI are depicted in Fig. 1C, revealing sharp diffraction peaks at 2θ values of 11.6°, 24.3° and 27.9° for HPI, which indicate its exceptional crystallinity. The well-crystalline nature can be attributed to the polymer segments' rigid chain structure and high conjugation level [33].

The HPI-Ti was fabricated by spin coating with the HPI slurry (Fig. 1A), followed by heat treatment. A commendable binding ability of HPI coating was verified by scratch testing and ultrasonic peeling method (Fig. S1). The representative SEM image of HPI-Ti exhibits the characteristic narrow needle-like morphology of HPI (Fig. 1D). FTIR spectra are depicted in Fig. 1E, in which characteristic FTIR peaks corresponding to HPI are observed in HPI-Ti. It indicates that HPI coating has been successfully fabricated on titanium surfaces, preserving its inherent morphology and structural integrity.

2.2. Electrochemical properties and charge/discharge mechanism

The electrochemical redox activity of HPI-Ti is of significant

importance. Herein, an investigation into the charge transfer mechanism was conducted by recording the cyclic voltammetry (CV) curve of HPI-Ti. The CV curve in Fig. 2A reveals two reduction peaks at -0.50 V and -0.97 V [versus saturated calomel electrode (SCE)], indicating a stepwise charge storage mechanism. Three oxidation peaks are observed at -0.80 V (split into two peaks at -0.84 V and -0.79 V), -0.30 V, and -0.14 V (versus SCE), which can be attributed to charge release. Furthermore, the redox reaction kinetics of HPI-Ti were investigated using CV measurements with different scan rates (1 – 10 mV s^{-1}). As shown in Figs. S2a–c, slight changes in shape and peak shifts were observed in the CV curves at various scan rates, with b values of 0.73 and 0.86 for the two reduction peaks, respectively, indicating a surface-controlled redox reaction [38]. The galvanostatic charge and discharge (GCD) curves are illustrated in Fig. 2B, wherein the voltage plateau signifies the storage and release of charges within HPI-Ti. Utilizing the rechargeable nature of HPI-Ti, the post-charging HPI-Ti, including HPI-Ti-1 and HPI-Ti-2, were prepared, which were charged to different potential thresholds, -0.7 V and -1.0 V (versus SCE), respectively (Fig. S3).

The formation of electron-carried anion and dianion (HPI^- and HPI^{2-}) in post-charging HPI-Ti is reflected in Raman spectra (Fig. 2C). The characteristic Raman vibration modes of HPI-Ti at 1302, 1375, and 1571 cm^{-1} are observed that attributed to the aromatic core's C–C stretching and C–H bending, while the vibration modes at 1302 cm^{-1} exhibit a shift to 1291 cm^{-1} and 1289 cm^{-1} in HPI-Ti-1 and HPI-Ti-2, respectively, indicating the formation of electron-carried anion and dianion (HPI^- and HPI^{2-}). To be specific, the vibration mode at 1289 cm^{-1} belongs to the blended signal of HPI^- and HPI^{2-} , denoted as $A'(-1, -2)$; the vibration mode at 1302 cm^{-1} and 1375 cm^{-1} belongs to the HPI neutral molecules, denoted as $A'(0)$; the vibration mode at 1571 cm^{-1} belongs to HPI^- and neutral molecules, denoted as $A'(-1, 0)$ [39]. For HPI-Ti-1 and HPI-Ti-2, the ratio of $I_{A'(-1, -2)}/I_{A'(0)}$ increases from 0.85 to 0.89 (Table S1), ascribed to more production of HPI^- and HPI^{2-} . The formation of HPI anions and dianions in post-charging HPI is also demonstrated in UV–vis spectra (Figs. S4 and S5).

Notably, post-charging HPI-Ti exhibits electron transfer when immersed in an aqueous solution. As shown in Fig. 2D, HPI-Ti

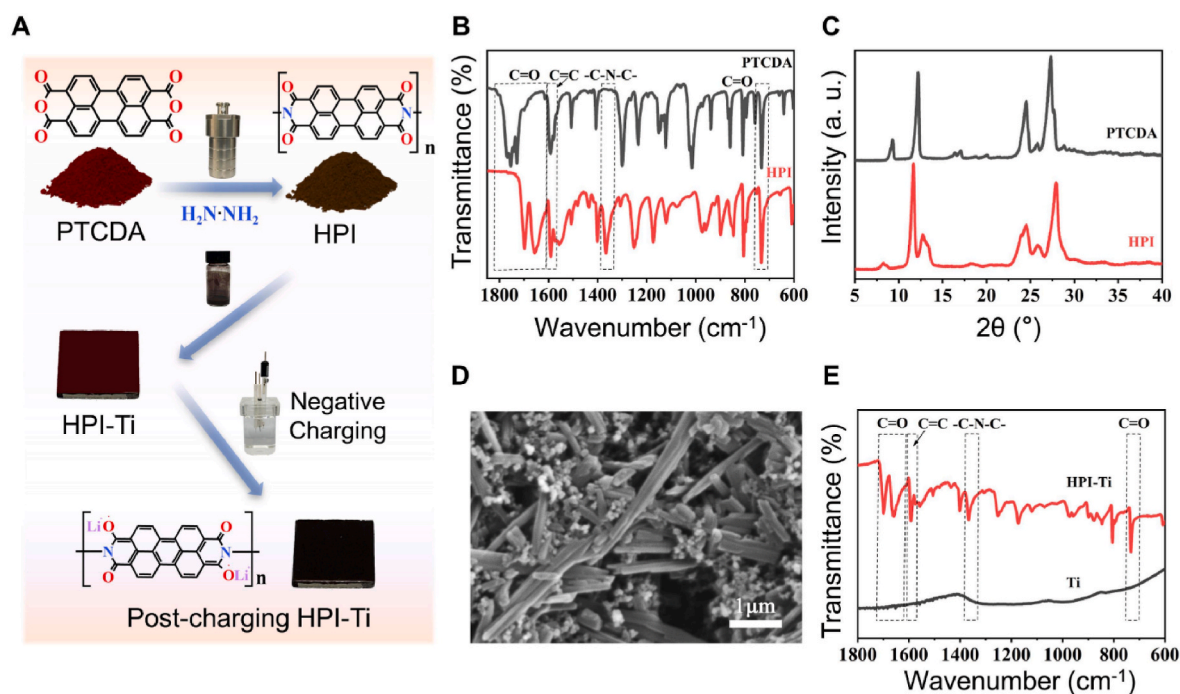


Fig. 1. Preparation and characterization of HPI and HPI-Ti. (A) Schematic illustration of the synthesis process for HPI, HPI-Ti, and post-charging HPI-Ti. (B) FTIR spectra and (C) XRD patterns of HPI and its raw material of PTCDA. (D) Representative SEM images of HPI-Ti. (E) FTIR spectra of Ti and HPI-Ti.

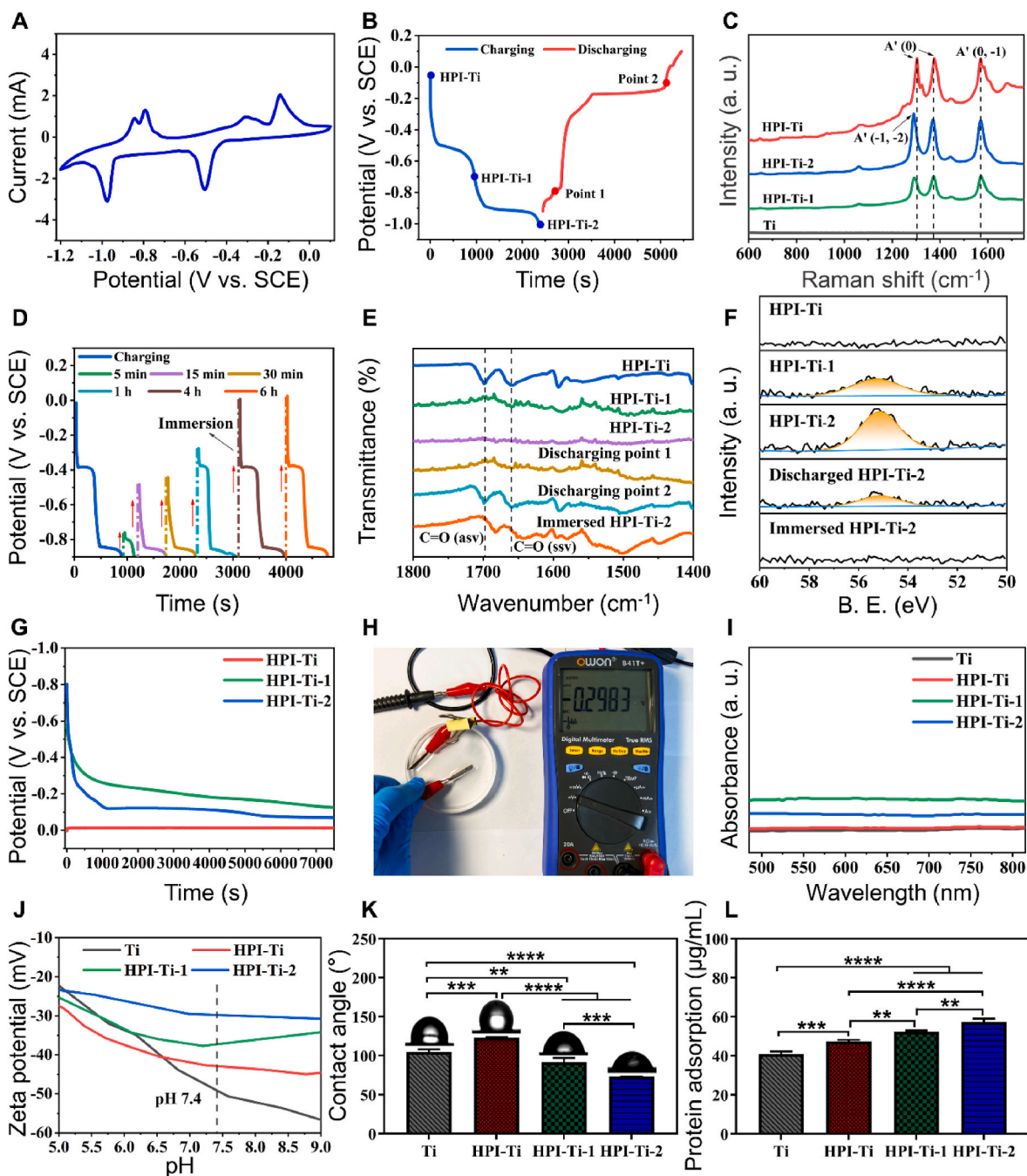


Fig. 2. Electrochemical properties, charge/discharge mechanism, and the associated surface properties. (A) Cyclic voltammetry (CV) curve of HPI-Ti in 1 M LiCl aqueous solution with a scan rate of 10 mV s^{-1} . (B) The galvanostatic charge and discharge (GCD) curve of HPI-Ti. (C) Raman spectra of Ti, HPI-Ti, HPI-Ti-1 and HPI-Ti-2. (D) Voltage-time curves of HPI-Ti with negative charging at 1 A g^{-1} after immersion in physiological saline for different durations. (E) Ex-situ FTIR spectra of HPI-Ti at different charging/discharging statuses marked in Fig. 2B and HPI-Ti-2 after immersion for 24 h. (F) Li 1s XPS high-resolution spectra of HPI-Ti, HPI-Ti-1, HPI-Ti-2, discharging HPI-Ti-2, and 24-h immersed HPI-Ti-2. (G) Open circuit potential of HPI-Ti, HPI-Ti-1, and HPI-Ti-2. (H) Optical image of the electric potential of HPI-Ti-2 in physiological saline. (I) The UV-Vis spectrum of the surface-catalyzed TMB colorimetric reaction of Ti, HPI-Ti, HPI-Ti-1, and HPI-Ti-2. (J) Zeta potential, (K) contact angle, and (L) surface protein adsorption of Ti, HPI-Ti, HPI-Ti-1, and HPI-Ti-2. Data are presented as mean \pm SD ($n = 3$). Statistical significance is indicated by asterisks: * $p < 0.05$, ** $p < 0.01$, *** $p < 0.001$, and **** $p < 0.0001$.

underwent charging (as indicated by the initial solid curve) and was then disconnected from the power supply. Subsequently, it was immersed in physiological saline, resulting in a gradual return of the open circuit potential (OCP) of HPI-Ti to its pre-charged state (as depicted by the dashed lines). A longer period of immersion results in a more complete recovery of OCP (as depicted by the dashed lines). This phenomenon may be attributed to the conformational transition in polyimides [36,40].

Further, the reaction mechanism of the conformation transition is investigated through ex-situ FTIR and XPS testing. The FTIR spectra are depicted in Fig. 2E. Peaks at 1700 and 1660 cm^{-1} represent C=O asymmetric and symmetric stretching vibration for HPI-Ti. For HPI-Ti-1 and HPI-Ti-2, the characteristic peaks of C=O bonds become weaker or even indiscernible. In contrast, for samples discharging to point 1 and point 2 (marked in Fig. 2B), the characteristic peaks of C=O bonds are gradually strengthened again, and the peaks are also observed in

immersed HPI-Ti-2, which are immersed in saline solution for 24 h. The enolization transformation in carbonyl groups has also been proved by XPS measurement, as presented in Fig. S6. Li 1s XPS spectra of different samples are shown in Fig. 2F. Li 1s peak at 55.1 eV appears in HPI-Ti-1 and HPI-Ti-2, and the peak area increases from HPI-Ti-1 to HPI-Ti-2, indicating lithium insertion during charging. The peak area of Li 1s diminishes in discharged HPI-Ti-2 and immersed HPI-Ti-2, showing the de-insertion of lithium ions during discharging and immersion. The total amount of lithium ions released measured by ICP-AES from HPI-Ti-1 and HPI-Ti-2 are 0.88 ppm and 1.31 ppm, respectively (Fig. S7). The release of charge carriers and conformation transition of post-charging HPI-Ti during galvanostatic discharge and immersion exhibit remarkable similarities, suggesting that immersion is a chemical potential-driven pathway for discharge.

To summarize, upon charging of HPI-Ti with negative current, the conjugated aromatic HPI molecules with carbonyl groups facilitate electron delocalization, resulting in the formation of electron-carried anions and dianions, and then stabilize through intercalation of Li^+ ions (considered as enol-form structure, $\text{R-C-O}^-\text{Li}^+$). The “chemical discharging” process is activated when immersed in physiological saline. Li^+ ions diffuse across the solid-liquid interface driven by a concentration gradient. Meanwhile, the enol-form (R-C-O^-) of HPI-Ti undergoes a conformational transition and reverts back to its keto-form (R-C=O).

2.3. Surface characterization

The changes in surface properties among Ti, HPI-Ti, HPI-Ti-1, and HPI-Ti-2 would influence the cellular/bacterial behaviors. Firstly, as the chemical discharging is activated by immersion, the open circuit potential (OCP) varies over time (Fig. 2G). The open circuit potential (OCP) of HPI-Ti-2 exhibits a rapid transition from -0.8 V to -0.1 V (versus SCE) within approximately 1000 s, followed by a decelerating fluctuation. Compared with HPI-Ti-2, the OCP of HPI-Ti-1 displays a narrower variation range, and the OCP of HPI-Ti remains essentially unaltered. Additionally, Fig. 2H visually illustrates the electrochemical activity of the post-charging HPI surface in a physiological environment by depicting the electric potential between HPI-Ti-2 and physiological saline. The UV-vis spectra of the surface-catalyzed 3,3',5,5'-tetramethylbenzidine (TMB) colorimetric reaction for different samples are illustrated in Fig. 2I, demonstrating no production of reactive oxide species on the surface.

Subsequently, the zeta potential, surface wetting, and protein adsorption properties vary after charging. Zeta potential plays a crucial role in protein adsorption and cell adhesion, and the surface potential at $\text{pH} = 7.4$ was considered as the reference value for the physical environment. The corresponding surface zeta potentials of Ti, HPI-Ti, HPI-Ti-1, and HPI-Ti-2 at $\text{pH} = 7.4$ are -52 mV, -42 mV, -37 mV, and -30 mV, respectively (Fig. 2J). Zeta potentials of HPI-Ti-1 and HPI-Ti-2 exhibit a positive shift trend compared with HPI-Ti. Surface wetting properties were analyzed, and the results are presented in Fig. 2K. The water contact angle of Ti is approximately 100° . Due to the hydrophobic nature of HPI, a type of perylene polyimides, the contact angle of HPI-Ti increases to 120° . However, HPI-Ti-1 and HPI-Ti-2 show smaller contact angles, with 90° for HPI-Ti-1 and 60° for HPI-Ti-2. Furthermore, Fig. 2L demonstrates increased protein adsorption levels from Ti, HPI-Ti, and HPI-Ti-1 to HPI-Ti-2, which will promote cell adhesion. In contrast to the smoother surface morphology of Ti, HPI-Ti, HPI-Ti-1, and HPI-Ti-2 exhibit a narrow needle-like morphology (Fig. S8). Therefore, the differences in surface properties among HPI-Ti, HPI-Ti-1, and HPI-Ti-2 can be attributed to the conformation transition involved in the charging process.

2.4. Antibacterial activity and electron transfer mechanism

Gram-positive *S. aureus* and Gram-negative *E. coli* were chosen to investigate the antibacterial activity of various samples. Compared with

Ti, bacterial colonies of *S. aureus* are significantly reduced from HPI-Ti-1 and HPI-Ti-2, while lots of *S. aureus* colonies can still be found from HPI-Ti (Fig. 3A). It indicates that HPI-Ti-1 and HPI-Ti-2 show good antibacterial activities against *S. aureus*, while Ti and HPI-Ti do not. Live/dead staining was conducted to investigate the biofilm formation of *S. aureus* on various samples further. As a result, Ti and HPI-Ti exhibit vivid green fluorescence (Fig. 3B), indicating the accumulation of abundant live *S. aureus* to form biofilm. However, the green fluorescence decreases and is accompanied by red fluorescence in HPI-Ti-1. Almost no green fluorescence and a higher amount of red fluorescence can be observed from HPI-Ti-2, indicating prevention of biofilm formation on post-charging HPI-Ti. The inhibitory effects on biofilm formation can also be observed in the representative SEM images and biofilm viability analysis (Figs. S9a and b). The quantitative survival rates of *S. aureus* were calculated based on the agar plate count analysis, and the results are shown in Fig. 3C. Compared with Ti, the antibacterial rates of *S. aureus* from HPI-Ti-1 and HPI-Ti-2 groups increase, and the antibacterial rate of HPI-Ti-2 against *S. aureus* is 99.96 ± 0.01 % for 24 h, suggesting a remarkable antibacterial efficiency. The antibacterial efficacy increases as the charging capacitance is elevated from HPI-Ti-1 to HPI-Ti-2.

Relevantly, the mechanism associated with antibacterial efficacy against *S. aureus* was investigated. To begin with, an interesting reversible change in antibacterial activity against *S. aureus* is observed in Fig. 3D. In detail, photographs of d1, d2, d3, and d4 represent the corresponding bacterial agar plate of HPI-Ti, post-charging HPI-Ti, chemical discharged HPI-Ti, and recharged HPI-Ti. It suggests that the antibacterial activity of HPI-Ti is activated through charging, deactivated after chemical discharging, and renewed upon recharging. Further, antibacterial rates and efficiency after coculturing with HPI-Ti-2 for 0, 0.5, 1, 2, and 4 h are profiled in Fig. 3E and F. The antibacterial rate of *S. aureus* in HPI-Ti-2 samples gradually increases, with the bacterial inhibition rate at 99.63 ± 0.13 % for 6 h (Fig. 3E). Notably, the antibacterial efficiency exhibits a rapid surge within the time frame of 0.5–1 h, reaching its peak value in 1 h with an impressive antibacterial efficiency of 24.80 ± 2.96 % per hour (Fig. 3F). Furthermore, the most significant alteration of discharging potential in HPI-Ti-2 inoculated with *S. aureus* is observed during this timeframe, indicating an active charge transfer on its surface. Subsequently, during the 1–6 h, although the antibacterial rate continues to rise, the antibacterial efficiency diminishes, then tends to stabilize, exhibiting a pattern similar to that observed in potential variation, thus verifying the correlation between surface charge transfer and antibacterial effects.

Furthermore, the representative SEM morphology of *S. aureus* cultured on HPI-Ti-2 for 0–6 h was investigated to capture more details about the interaction between *S. aureus* and HPI-Ti-2. As shown in Fig. 3G, at the beginning, *S. aureus* inoculated on the sample surface remains intact cell membrane and exhibits a spherical shape. After half an hour, the cell membranes of some bacteria become crumpled. More crumpled cell membranes can be observed for longer co-culture time, and significant damage of cell membranes, including cytosolic content leakage, membrane perforation, and curl distortion, is observed for 1, 2, 4, and 6 h. Moreover, the damage of the bacteria membrane potentials is observed in the fluorescence images of the CTC assay (Fig. S10). The variation in total ATP amount and intracellular ROS levels is vital in bacterial energy metabolism. As is shown in Fig. 3H, the total ATP amount sharply decreases for HPI-Ti-1 and HPI-Ti-2 compared with Ti and HPI-Ti. The intracellular ROS levels of HPI-Ti-2 significantly increase compared with the other three groups (Fig. 3I). The close interaction between bacteria and materials results in the impairment of bacterial membrane integrity, a reduction in total ATP levels, and an increase in intracellular ROS. Additionally, the absence of a ROS signal in the materials (Fig. 2I) suggests that bacterial intracellular oxidative stress is induced by their interaction with the post-charging HPI-Ti surface rather than generated by the materials.

Compared with cocultured directly on the material's surface, no

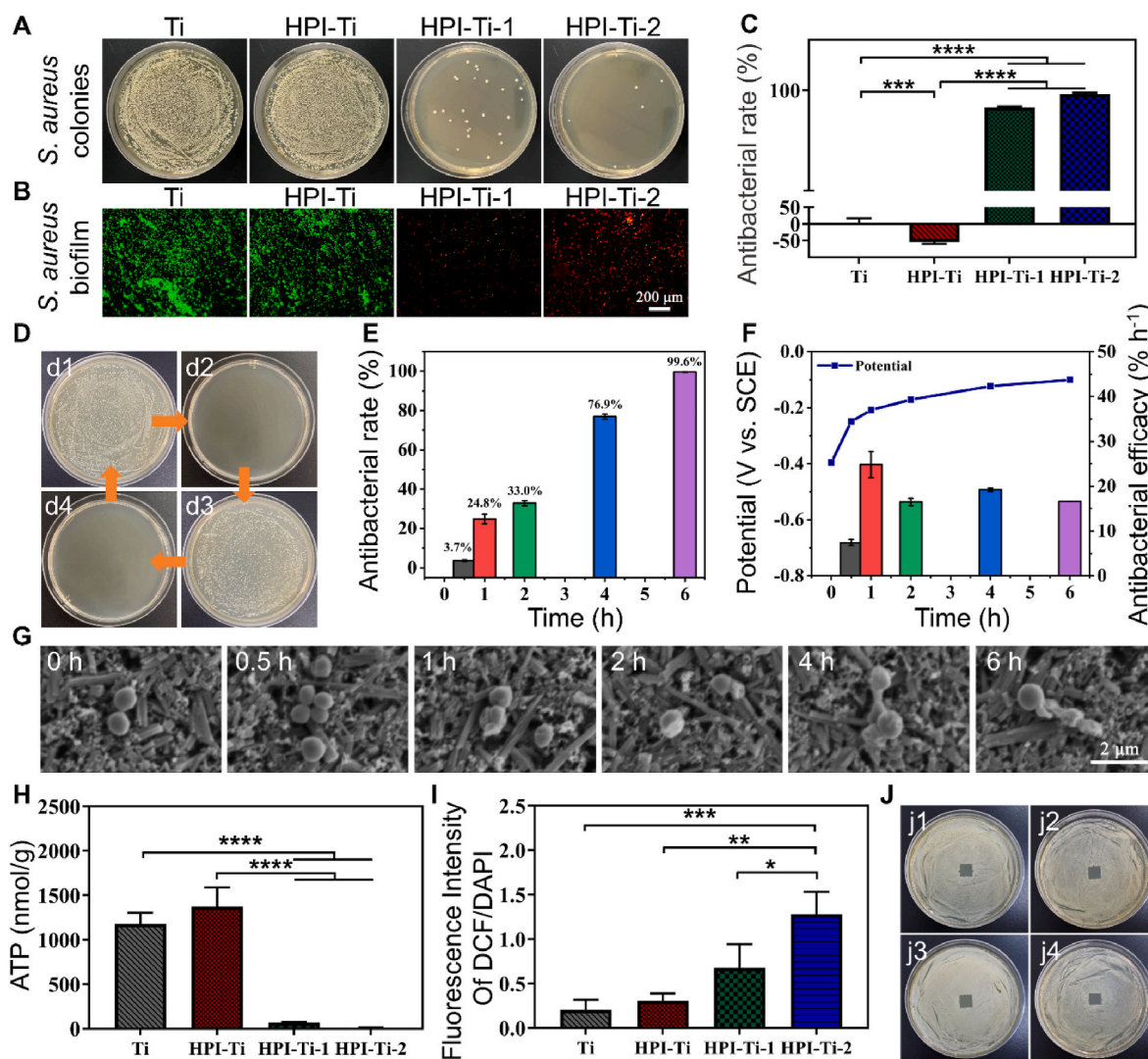


Fig. 3. Antibacterial effects against *S. aureus*. (A) Representative agar plate photographs of *S. aureus* colonies from Ti, HPI-Ti, HPI-Ti-1, and HPI-Ti-2. (B) Live/dead staining fluorescence images of *S. aureus* biofilm on Ti, HPI-Ti, HPI-Ti-1, and HPI-Ti-2. (C) Antibacterial rate of Ti, HPI-Ti, HPI-Ti-1, and HPI-Ti-2 against *S. aureus*. (D) Renewable antibacterial activity of HPI-Ti against *S. aureus* (d1, d2, d3, and d4 represent the corresponding bacterial agar plate of HPI-Ti, post-charging HPI-Ti, discharged HPI-Ti, and recharged HPI-Ti). (E) Inhibition rates of *S. aureus* cultured on HPI-Ti-2 for 0.5, 1, 2, 4, and 6 h. (F) Antibacterial efficiency and discharging potential of HPI-Ti-2 inoculated with *S. aureus* for various durations. (G) Representative morphology of *S. aureus* cocultured on HPI-Ti-2 for 0–6 h. (H) Total ATP amount of *S. aureus* from various samples. (I) Intracellular ROS levels of *S. aureus* from various samples. (J) Representative agar plate photographs of inhibition ring against *S. aureus* from various samples (j1, j2, j3, and j4 represent Ti, HPI-Ti, HPI-Ti-1, and HPI-Ti-2). Data are presented as mean \pm SD ($n = 3$). Statistical significance is indicated by asterisks: * $p < 0.05$, ** $p < 0.01$, *** $p < 0.001$, and **** $p < 0.0001$.

inhibition rings against *S. aureus* are observed in the agar diffusion assay of Ti, HPI-Ti, HPI-Ti-1, and HPI-Ti-2. (Fig. 3J). Moreover, *S. aureus* cocultured in the extractions from each sample is not inhibited (Fig. S11). These findings suggest that the release of Li^+ ions and other potential changes in the culturing medium poses little threat to the survival of *S. aureus*, and close contact is required in the interaction between the bacteria and post-charging HPI-Ti.

Similar experiments were conducted using *E. coli*, but the results differ from those of *S. aureus*. There is no significant difference in antibacterial rate among Ti, HPI-Ti, HPI-Ti-1, and HPI-Ti-2 samples in Fig. 4A. Further, As presented in Fig. 4B, the total ATP amount of *E. coli* from HPI-Ti-2 shows a slightly downward trend, while changes among Ti, HPI-Ti, and HPI-Ti-1 groups are negligible, suggesting a limited influence on the energy metabolism of *E. coli*. As displayed in Fig. 4C, no significant changes are observed in intracellular ROS levels among all the samples. Lots of red and blue fluorescence can be seen in CTC staining fluorescence images from all the samples, indicating intact cell membrane potential (Fig. S12). As shown in Fig. 4D, lots of bacterial

colonies are observed from Ti, HPI-Ti, HPI-Ti-1, and HPI-Ti-2, and green fluorescence can be seen in live/dead assay from Ti, HPI-Ti, HPI-Ti-1, and HPI-Ti-2 (Fig. S13), verifying the present post-charging samples exert little impact on the survival of *E. coli*. Why is it ineffective against *E. coli*? To enhance the antibacterial effect against *E. coli*, we increased the HPI content on titanium and charged it to -1.0 V (consistent charging parameters as HPI-Ti-2). Consequently, the bacterial colonies reduce, and the antibacterial rates increase as the amount of HPI on titanium increases from 0.1 mg to 0.2 mg and 0.3 mg after charge (Fig. 4E and F), accompanied by inhibition of ATP synthesis and an accumulation of ROS (Fig. 4G and H). The differential antibacterial efficacy against *S. aureus* and *E. coli* can be attributed to the variations in their membrane structure and associated functions [41,42]. *S. aureus* is a type of Gram-positive bacteria with a bacterial membrane consisting of layers of peptidoglycan and a single-layered inner membrane (IM), lacking an outer membrane (OM); *E. coli* is a type of Gram-negative bacteria with a bacterial membrane consisting of the OM, the peptidoglycan cell wall, and the IM, which is more complex than that of

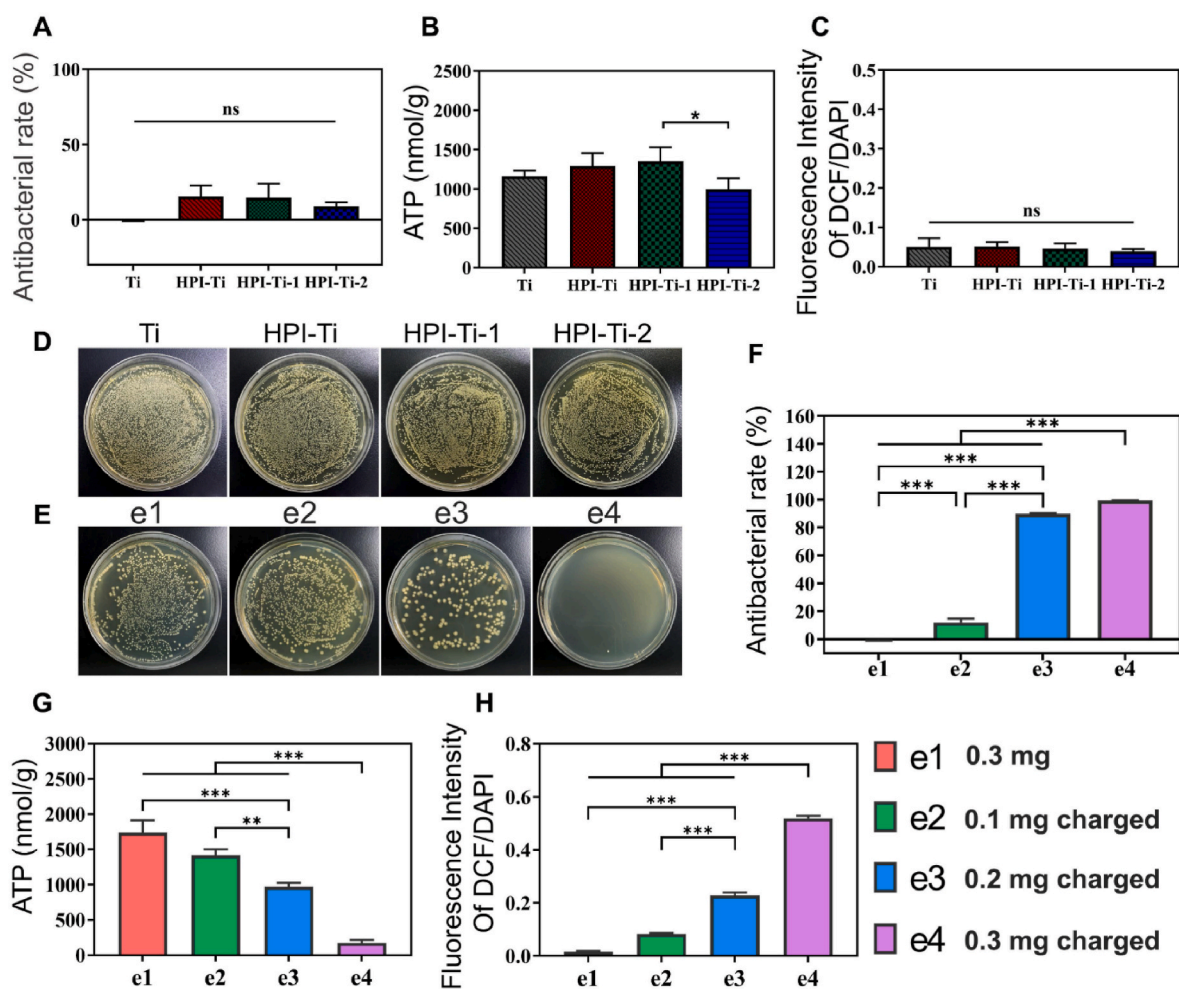


Fig. 4. Antibacterial effects against *E. coli*. (A) Antibacterial rate of Ti, HPI-Ti, HPI-Ti-1, and HPI-Ti-2 against *E. coli*. (B) Total ATP amount of *E. coli* from various samples. (C) Intracellular ROS levels of *E. coli* from various samples. (D) Representative agar plate photographs of *E. coli* from Ti, HPI-Ti, HPI-Ti-1, and HPI-Ti-2. (E) Representative agar plate photographs of *E. coli* cultivated with (e1) 0.3 mg HPI-Ti, (e2) 0.1 mg charged HPI-Ti, (e3) 0.2 mg charged HPI-Ti, and (e4) 0.3 mg charged HPI-Ti. (F) Antibacterial rates, (G) total ATP amount, and (H) intracellular ROS levels of *E. coli* with increasing HPI content on titanium corresponding to the samples in Fig. 4E. Data are presented as mean \pm SD ($n = 3$). Statistical significance is indicated by asterisks: * $p < 0.05$, ** $p < 0.01$, *** $p < 0.001$, and **** $p < 0.0001$.

S. aureus [43].

The electron-transfer interaction between bacteria and material was further investigated electrochemically. As shown in Fig. 5A and B, the colonization of *S. aureus* and *E. coli* on the material surface leads to variations of peak position and peak current at -0.5 V (versus SCE) in I–V curves, which remain unchanged in CV cycles of HPI-Ti-2 without bacteria (Fig. S14). Moreover, the bacteria-associated electrical signal in I–V curves is investigated in repeated tests (Fig. S15 for *S. aureus* and Fig. S16 for *E. coli*); compared to *S. aureus*, *E. coli* colonization leads to a more significant peak current variation (Fig. 5C).

Additionally, electrochemical impedance spectroscopy (EIS) was conducted on bacteria-inoculated HPI-Ti-2. According to EIS Nyquist curves, compared to HPI-Ti-2, the radii of impedance arcs exhibit a slight decrease with live *S. aureus* (Fig. 5D) and a significant reduction with live *E. coli* (Fig. 5E). In the phase angle plot (Figs. S17 and 18), two peaks at approximately 0.1 Hz (corresponding to the slow mass transfer) and 1000 Hz (corresponding to the quick responsive electron transfer process) can be detected from the HPI-Ti-2, as well as HPI-Ti-2 with/without bacteria (*S. aureus* and *E. coli*). Thus, an equivalent circuit model with capacitive elements, charge transfer resistance, and Warburg impedance is used to fit the EIS data of these samples (Fig. 5F), in which R_s represents the resistance of the electrolyte solution, R_{film} represents the resistance of the bacteria film, Z_w represents the Warburg impedance, R_{ct} represents the charge transfer resistance between the hybrid

film (HPI coating and the bacteria film) and the electrolyte, Q_{film} represents the capacitive constant phase element of the hybrid film, and Q_i represents constant phase element at the interface between the titanium substrate and electrolyte. According to the fitted results by the EIS equivalent circuit model, the influence of *S. aureus* on the electron transfer impedance (R_{ct}) within HPI-Ti-2 is minor, decreasing from 1.046×10^3 to 8.152×10^2 ; the electron transfer impedance (R_{ct}) with live *E. coli* changes significantly, falling from 1.164×10^3 of HPI-Ti-2 to 9.517×10^1 of HPI-Ti-2 with live *E. coli* (Tables S2 and S3). Notably, the presence of dead bacteria (*S. aureus* and *E. coli*) results in a reduction in peak current and an elevation in R_{ct} , suggesting that only live bacteria contribute to the electron transfer within the material. The slight decrease in total ATP of *E. coli* observed in HPI-Ti-2 indicates that the metabolic activity of *E. coli* remains intact mainly, thereby contributing more electrons and resulting in a more significant electrical signal.

Fig. 5G illustrates the interaction between bacterial and post-charging HPI. Bacteria accomplish the process of electron transfer in the respiratory chain and synthesize ATP through enzyme complexes located on the membrane. This intricate process involves the sequential transport of electrons from NADH/FADH₂, coenzyme Q, and cytochromes to a specific electron acceptor via enzyme complexes and their associated cofactors situated on or near the bacterial inner membrane [44,45]. In our experiments, the bacterial membrane is in contact with the post-charging HPI surface, where the oxygen atom with lone pair

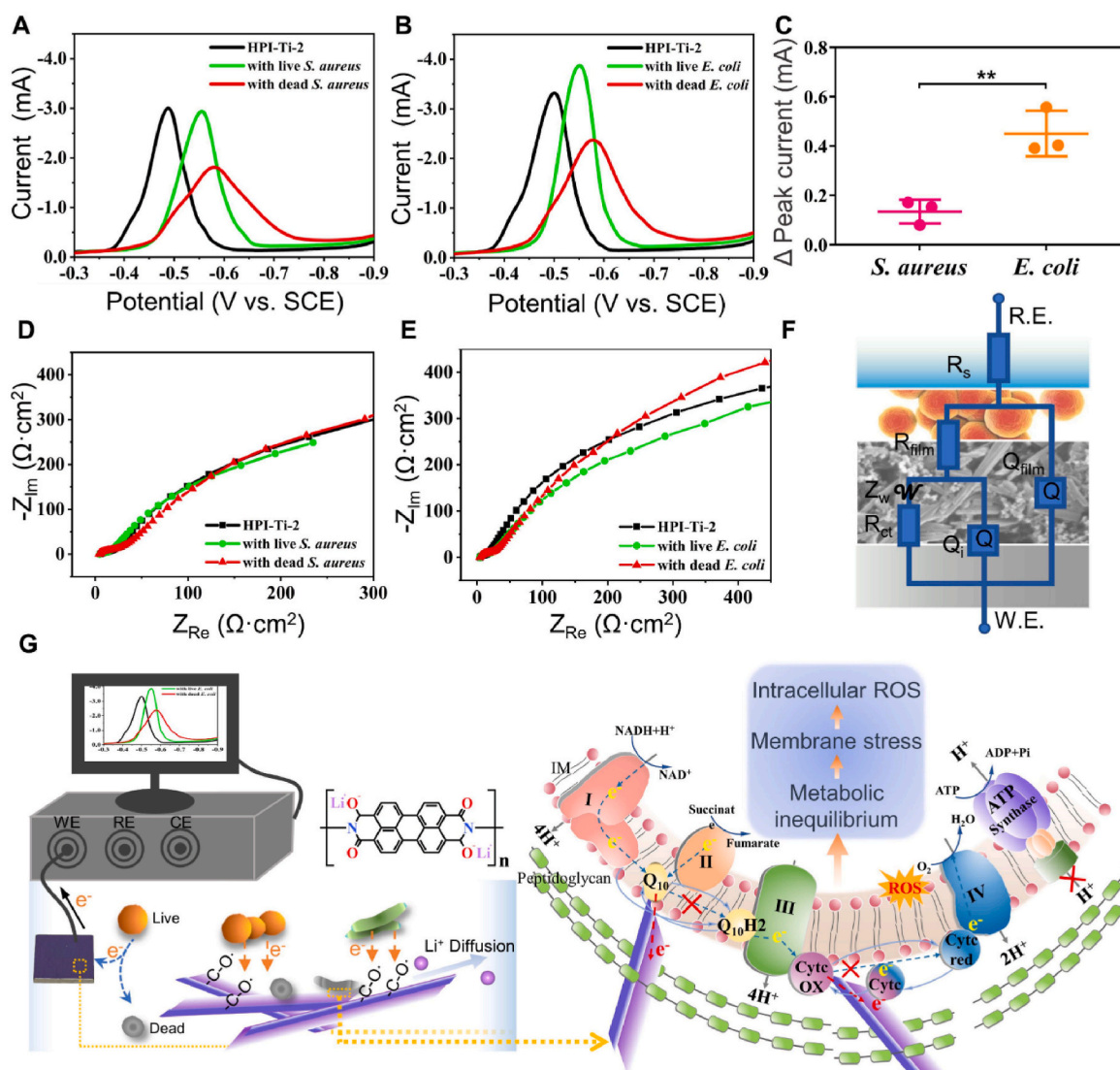


Fig. 5. Electron-transfer interactions and the underlying antibacterial mechanism. I–V curves of HPI-Ti-2 before/after inoculation with live/dead (A) *S. aureus* and (B) *E. coli*. (C) Peak current variations of HPI-Ti-2 at around -0.5 V after inoculation with live *S. aureus* and *E. coli*. EIS Nyquist plots of HPI-Ti-2 before/after inoculation with live/dead (D) *S. aureus* and (E) *E. coli*. (F) Schematic illustration of the equivalent circuit model for EIS analysis of HPI-Ti-2 before/after inoculation with bacteria (*S. aureus* and *E. coli*). (G) Schematic illustration of electrical signal tests and electron-transfer mechanism between bacteria and material. Data are presented as mean \pm SD ($n = 3$). Statistical significance is indicated by asterisks: * $p < 0.05$, ** $p < 0.01$, *** $p < 0.001$, and **** $p < 0.0001$.

electron in enol-form π -conjugated HPI molecular is electron withdrawing, thus altering the normal ET pathway marked by blue dash arrows to the ones shown by red arrows in Fig. 5G. Further, the snatched electrons are delocalized through the π -conjugated electric channel triggered by the enol-keto transition, enter the Ti substrate, and produce electrical signals observed in Fig. 5A and B. Consequently, the impaired transmembrane transport of substances and energy in bacteria leads to membrane stress, followed by inhibited adenosine triphosphate (ATP) synthesis and intracellular reactive oxygen species (ROS) accumulation.

2.5. Fibroblast response

Fibroblasts undertake essential roles in soft tissue integration. Accordingly, we paid close attention to the influence of various samples on human gingival fibroblasts (HGFs) response. Cell adhesion in the initial stage of biomaterial-host cell interaction plays a considerable role and will influence the following cell behaviors: proliferation, migration, and differentiation. Fig. 6A shows the initial cell adhesion of HGFs on various samples. After 1 h, HGFs on the surface of all the samples show a

round morphology with few cells starting to spread out, and HGFs on HPI-Ti-2 show better adhesive behavior and the largest spreading area than the other groups. After 4 h, the spreading area of HGFs extends, and cell morphology differs among groups. Plenty of cells on Ti and HPI-Ti-2 exhibit polygonal shapes, while cells on HPI-Ti and HPI-Ti-1 show elongated morphology with lots of lamellipodia. When incubated for 24 h, the widely spreading cytoskeleton is seen on all the samples. In the semi-quantitative analysis, the cell spreading area of FTIC-stained cytoskeleton in HGFs cultured on HPI-Ti-1 and HPI-Ti-2 exhibited a significant increase compared to that observed on Ti (Fig. S19). It suggests that fibroblast adhesion is promoted in the initial discharge stage.

Cell proliferation was investigated, and the results are presented in Fig. 6B. The cell proliferation for 1, 3, and 5 days shows an overall upward trend for all the samples. No significant difference is observed in 1 day. In contrast, a substantial improvement of proliferation levels is observed from HPI-Ti, HPI-Ti-1, and HPI-Ti-2 compared to Ti at 3 and 5 days, indicating an enhanced cell proliferation as the temporal-sequence regulated post-charging model enters the later discharging stage after 1 day.

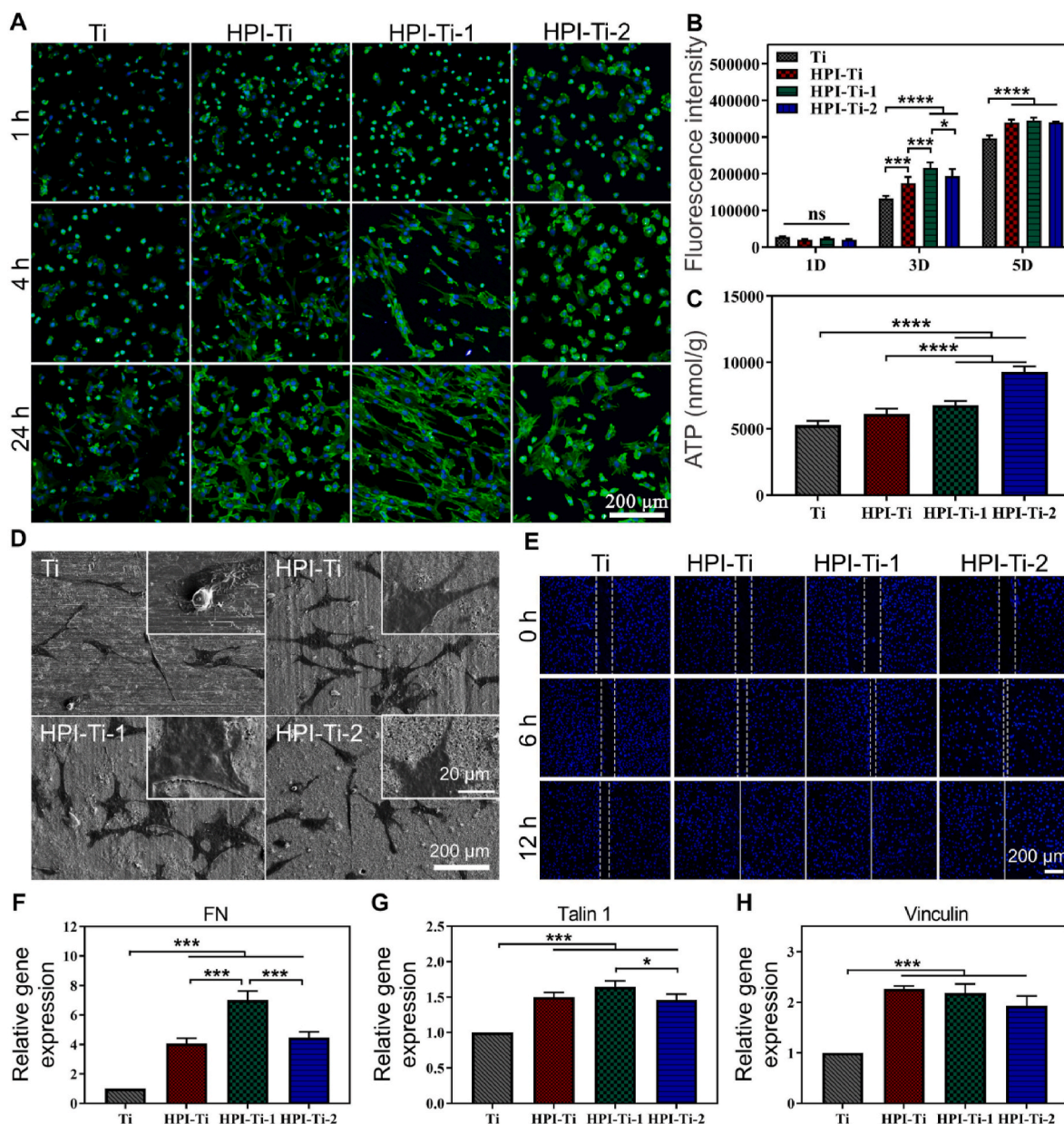


Fig. 6. Fibroblast response *in vitro*. (A) Cytoskeleton-staining fluorescence images of HGFs cultured with various samples for 1, 4, and 24 h. (B) Proliferation of HGFs cultured with various samples for 1, 3, and 5 days. (C) The total amount of intracellular ATP of HGFs cultured with various samples for 1 day. (D) Representative SEM image of HGFs culturing on various samples for 1 day. (E) Fluorescence images of HGFs with nuclei stained by DAPI on various samples for 0, 6, and 12 h in wound healing assay. Relative expression level of adhesion-related genes of HGFs, including (F) FN, (G) Talin 1, and (H) Vinculin. Data are presented as mean \pm SD (n = 3). Statistical significance is indicated by asterisks: *p < 0.05, **p < 0.01, ***p < 0.001, and ****p < 0.0001.

The total intracellular ATP amount was measured to test the influence of energy metabolism for HGFs, and the results are shown in Fig. 6C. An improvement of total cellular ATP levels is observed from HPI-Ti-1 and HPI-Ti-2 compared with Ti and HPI-Ti, demonstrating that the post-charging surface does not inhibit cellular energy production. Cell morphology was further investigated by SEM. As shown in Fig. 6D, the spreading area of HGFs on Ti is the smallest, while HGFs in other groups exhibit lots of filopodia and lamellipodia, indicating improved cell adhesion and spreading effect. The migration of fibroblasts to the wound sites plays a significant role in soft tissue sealing. The wound healing assay depicted in Fig. 6E demonstrates that the migration of HGFs is enhanced on the surfaces of HPI-Ti-2 and HPI-Ti-1 compared to HPI-Ti and Ti. This finding aligns with previous studies indicating that electrical stimulation facilitates cell migration [30]. Additionally, live/dead staining results of HGFs cultured with various samples

indicate the absence of cytotoxicity in these samples (Fig. S20). Furthermore, the preferable cell adhesion, proliferation, and viability of mouse-derived fibroblasts (L929) are observed on post-charging HPI-Ti (Fig. S21-23).

The fibroblast response is regulated in different discharge stages. In the initial adhesion stage, the electrical stimulation on the post-charging HPI-Ti surface enhances cell adhesion and migration ability. The post-charging HPI-Ti demonstrates no cytotoxicity for extended coculture durations and promotes fibroblast proliferation on its surface. The cell morphology remains intact, and ATP synthesis is not inhibited. Regarding cells, the electron transfer of the respiratory chain is primarily completed within specialized organelles known as mitochondria [20]. Consequently, even if the cellular membrane directly contacts the material surface, its electron transfer chain remains unaffected. In contrast, the adhesion-related proteins and extracellular matrix (ECM)

proteins are localized in the vicinity of the cell membrane, rendering them susceptible to regulation by external signals at the interface between cells and materials. The qPCR experiment on HGFs revealed an upregulation in the expression of cell adhesion-related genes, including fibronectin (FN), Talin 1, and vinculin (Fig. 6F–H). FN is an ECM protein that functions in cell adhesion and migration by specifically binding cell adhesion molecules [46]. Talin is an essential mediator of integrin activation and cell anchorage [47]. Vinculin is essential in enabling mechanical coupling between the actin cytoskeleton and the ECM. Extracellular signals at the cell-material interface can be transmitted through dynamic remodeling of the actin cytoskeleton, which can influence cellular behaviors such as adhesion, migration, and proliferation [48].

2.6. Antibacterial activity and soft tissue compatibility *in vivo*

Bacterial infections can trigger severe inflammatory responses and destroy the natural organization of soft tissues, which are detrimental to soft tissue sealing. The ability to inhibit bacterial infections is vital to enhance soft tissue sealing in percutaneous implants. Therefore, the antibacterial efficiency and soft tissue compatibility were tested *in vivo*, and the operation procedure was illustrated in Fig. 7A. Given its good antibacterial properties (99.83 ± 0.01 % against *S. aureus* for 24 h), HPI-Ti-1 was selected as the treated group of post-charging material due to its advantages in enhancing cell adhesion and proliferation *in vitro* compared with HPI-Ti-2. *S. aureus* was inoculated with Ti, HPI-Ti, and HPI-Ti-1 for 2 h and placed subcutaneously in mouse dorsal skin. All mice remained healthy throughout the study, and no swelling or other complications related to the surgery were observed. The dorsal skin tissues with integrated samples were collected on days 1, 4, 7, and 14 after implantation. The antibacterial effect *in vivo* was then evaluated by the agar plate counting method and histological staining. On days 1 and 4, numerous bacterial colonies of *S. aureus* can be observed on Ti and HPI-Ti, while the presence of bacterial colonies on HPI-Ti-1 is negligible, especially on day 4 (Fig. 7B). It can be seen from the quantitative results in Fig. 7C that the antibacterial rate of HPI-Ti-1 against *S. aureus* at 4 days is 99.00 ± 0.01 %. Giemsa staining images are presented in Fig. 7D. After implantation for 1 day, the stained bacteria (indicated by arrows) can be observed from Ti and HPI-Ti while the bacteria sharply reduce from HPI-Ti-1. After 4 days, more bacteria are seen from Ti and HPI-Ti, indicating no antibacterial effect. However, the stained bacteria (indicated by arrows) can hardly be observed from HPI-Ti-1, suggesting an effective antibacterial ability *in vivo*.

Bacterial infiltration can lead to persistent and severe inflammation within the tissue, impeding the proper integration of soft tissue with the material. Hematoxylin & Eosin (H&E) staining is conducted on the tissue in contact with the materials, and the results are presented in Fig. 7E. Significant infiltration of inflammation can be seen from Ti and HPI-Ti at 4 days (indicated by circles), along with numerous inflammatory cells being observed (Fig. S24). The inflammatory response of HPI-Ti-1 is significantly suppressed compared to Ti and HPI-Ti, indicating that the inhibition of bacterial infection can effectively mitigate excessive inflammation.

Bacterial infiltration can significantly disrupt the inherent structure of soft tissue and collagen organization. Therefore, collagen deposition was further investigated using Masson's trichrome staining. It is evident from Fig. 7F that the positive-stained collagen fibers in HPI-Ti-1 are dense and well-organized, in contrast to the loose and disordered collagen fibers observed in Ti and HPI-Ti samples. Furthermore, enhanced collagen I expression at the material-tissue interface of the HPI-Ti-1 group is preferable to promote cellular adhesion and tissue integration at the interface, as shown in Fig. 7G (indicated by red arrows). It is suggested that HPI-Ti-1 can efficiently inhibit bacteria *in vivo* and facilitate soft tissue sealing. Additionally, no tissue damage is observed in H&E staining of the heart, liver, spleen, lung, and kidney (Fig. S25).

3. Conclusions

In summary, we have developed a rechargeable polyimide (HPI) coating on medical titanium (HPI-Ti) to realize the temporal-sequence regulation of antibacterial activity and soft tissue sealing. By adjusting the charging thresholds, post-charging HPI-Ti with different capacitances were prepared (HPI-Ti-1 and HPI-Ti-2). Discharge is initiated driven by chemical potential upon immersion in physiological saline. During the early discharge stage, HPI-Ti-2 demonstrates a 99.96 ± 0.01 % sustained antibacterial rate for 24 h and prevents biofilm formation. Furthermore, A strong correlation between antibacterial efficiency and discharge potential of bacteria-inoculated HPI-Ti-2 is observed. The bacteria-contributed electrical signal in the I–V curve and EIS of HPI-Ti-2 is tested. The temporal-sequence regulation of antibacterial activity and soft tissue sealing is achieved in different discharge stages (Scheme 2). In the initial adhesion stage, the violent electron transfer between bacteria and material has led to membrane impairment, inhibition of ATP synthesis, and accumulation of intracellular ROS in bacteria. Additionally, post-charging HPI-Ti enhances the adhesion and migration of fibroblasts. In the later discharge stage, the attenuated discharge status offers a more conducive environment for cellular growth. Consequently, post-charging HPI-Ti promotes the proliferation of fibroblasts *in vitro*, as well as facilitates soft tissue sealing *in vivo*. Moreover, recharging can potentially reinstate the antibacterial activity as a precautionary measure for potential reinfection. The systematic study on rechargeable HPI coating on titanium presents a tactic for designing temporal-sequence-regulated devices with enhanced antibacterial efficacy and soft tissue compatibility.

4. Experimental section

4.1. Preparation and characterization of HPI

Hydrazine hydrate-derived polyimide (HPI) was synthesized through the condensation reaction of perylene-3,4,9,10-tetracarboxylic dianhydride (PTCDA, Sigma-Aldrich Chemical, USA) and hydrazinium hydrate (Aladdin Industrial, China). In detail, 2 mmol of PTCDA, 2 mmol of hydrazinium hydrate, and 5.0 g of imidazole were mixed in a Teflon reactor and reacted at 140 °C for 5 h. Subsequently, the cooled mixture was treated with 1 M hydrochloric acid and stirred for 15 min. The precipitate was collected via vacuum filtration and washed with boiling saturated potassium carbonate solution, followed by multiple washes with distilled water and ethanol. The resulting product was then air-dried at 100 °C for 24 h and ground into a powder using a mortar. The FTIR spectrometer (Tensor 27, Bruker, Germany) was used to detect the absorption peaks of the samples in the range of 400–4000 cm^{-1} . X-ray diffraction patterns of the samples were obtained using a diffractometer (D2PHASE, BRUKER, USA).

4.2. Preparation and characterization of HPI-Ti

The commercial pure titanium (Ti) was cut into plates with 10 mm × 10 mm × 1 mm dimensions. Before use, the Ti plates underwent acid cleaning to remove surface contaminants. A homogeneous slurry was prepared by mixing 70 wt % HPI, 20 wt % carbon black, and 10 wt % PVDF (polyvinylidene fluoride, Sigma, USA) in N-methyl-2-pyrrolidone followed by stirring for 24 h. Then, the Ti plates were coated with the slurry using the spin coating method, achieving a mass loading of 0.1 mg cm^{-2} . Subsequently, the spin-coated Ti plates were subjected to thermal treatment at 100 °C for 10 h. The as-prepared samples were denoted as HPI-Ti. Subsequently, a different charging-state HPI-Ti was prepared by galvanostatic charging with an electrochemical workstation (PGSTAT302N, Metrohm Autolab, Switzerland). 1 M lithium chloride aqueous solution was employed as the electrolyte. A three-electrode electrolytic cell was used, wherein platinum foil and saturated calomel electrodes (SCE) were utilized as the counter and reference electrodes.

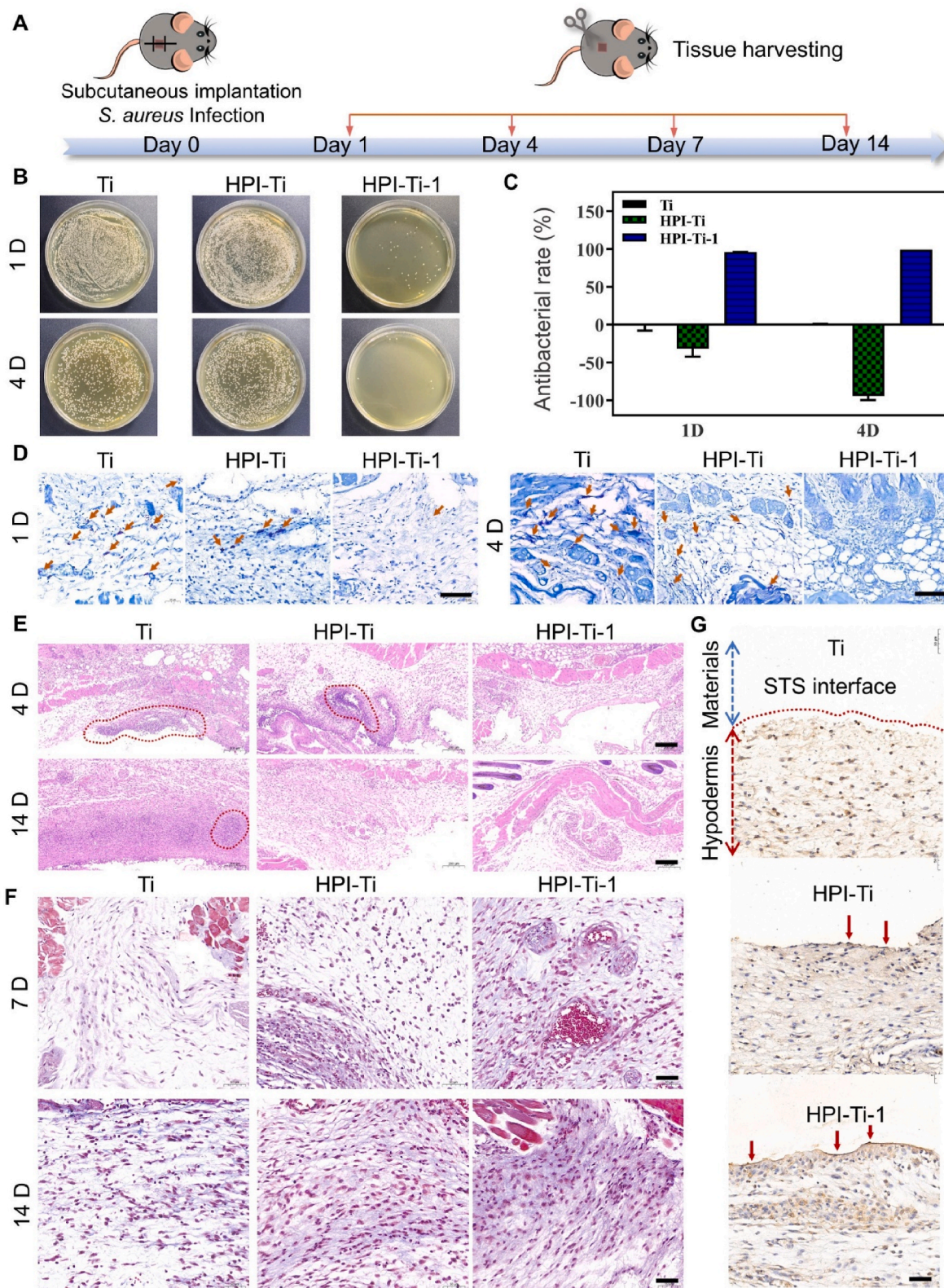
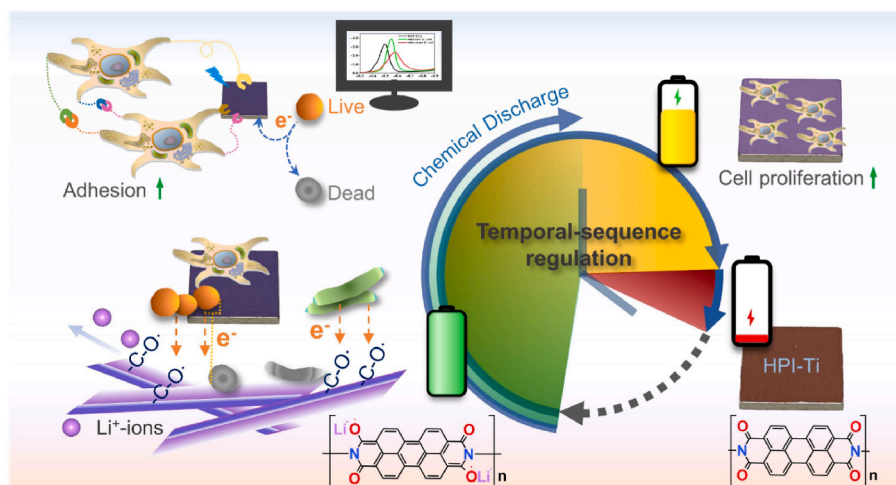


Fig. 7. Antibacterial activity and soft tissue compatibility *in vivo*. (A) Schematic diagram of animal experiments process. (B) Agar plate photographs and (C) corresponding quantitative statistics of bacteria colony counting from various samples. (D) Giemsa staining images from various samples after implantation for 1 and 4 days (scale bar: 100 μ m). (E) H&E staining after implantation for 4 and 14 days from various samples (scale bar: 200 μ m). (F) Masson's trichrome staining from various samples after implantation for 7 and 14 days (scale bar: 50 μ m). (G) Collagen I expression at the material-tissue interface after implantation for 14 days from various samples (scale bar: 50 μ m). Data are presented as mean \pm SD (n = 3).



Scheme 2. Schematic illustration of rechargeable HPI-Ti and the temporal-sequence regulation of antibacterial activity and soft tissue sealing.

The HPI-Ti sample was placed on the working electrode. During the charging process, the working current for galvanostatic charging is set to -0.8 mA. Charging is terminated when the potential threshold reaches -0.7 V and -1.0 V, designated as HPI-Ti-1 and HPI-Ti-2. It is worth noting that the collective term “post-charging HPI-Ti” encompasses both HPI-Ti-1 and HPI-Ti-2. The post-charging samples were rinsed in ultrapure water for 10 s to eliminate any residual electrolytes, followed by drying. The surface morphology of the samples was characterized using a scanning electron microscope (S-3400N, HITACHI, Japan). Raman spectra of various samples were detected using a Raman microscope (LabRAM, Horiba Jobin Yvon, France) with an Ar-ion laser for excitation at 514 nm. The absorption peaks of the samples in the range of $400\text{--}4000\text{ cm}^{-1}$ were detected using an FTIR spectrometer (Tensor 27, Bruker, Germany). The ultraviolet–visible near-infrared absorption spectra of the samples were determined using an ultraviolet–visible near-infrared spectrometer (Lambda 750, PerkinElmer, UK). The bonding ability between HPI coating and titanium substrate was tested using the scratch test with an MFT-4000 Multifunctional Tester for Material Surface (Lanzhou Huahui Instrument Technology Co., Ltd.). A diamond indenter (120° cone with a $200\text{ }\mu\text{m}$ hemispherical tip) was used for the scratch testing, with a load range of $0\text{--}100$ N. The loading was applied linearly at a loading rate of 100 N/min , and the scratch length was set at 5 mm .

4.3. Electrochemical analysis

The electrochemical behaviors of various samples were measured using an electrochemical workstation (PGSTAT302N, Metrohm Autolab, Switzerland) equipped with a three-electrode cell configuration. The reference electrode was a saturated calomel electrode (SCE); the working electrode consisted of the tested samples; a Pt foil was the counter electrode. The cyclic voltammetry (CV) experiments were conducted in the potential ranging from -1.2 V to 0.1 V vs. SCE at a scanning rate of 10 mV s^{-1} to obtain characteristic cyclic voltammograms. Additionally, cyclic voltammograms at different scan rates were performed for dynamic analysis. Electrochemical impedance spectra were detected from 0.1 Hz to 100 kHz with a sinusoidal signal of 10 mV amplitude. The galvanostatic charge/discharge experiments were performed with a current density of 1 A g^{-1} . The chemically discharging behavior was evaluated by immersing the post-charging HPI-Ti in saline without an external electrical source for various durations and then recharging it. The open circuit potentials of all the samples were tested in 0.9% NaCl solution (physiological saline).

The reaction mechanism of HPI-Ti occurring in the charging and chemical discharging process was evaluated through ex-situ FTIR and

XPS measurements. HPI-Ti-1 and HPI-Ti-2 were removed from the electrolytic cells. Immersed samples were prepared by immersing HPI-Ti-2 samples in $1\text{ mL } 0.9\%$ NaCl solution for 24 h. The residual electrolyte on the samples was absorbed by filter paper, followed by drying at 60°C for 3 h. Ex-situ FTIR measurements were conducted using attenuated total reflection mode. X-ray photoelectron spectroscopy (XPS; RBD upgraded PHI-5000C ESCA system, USA) was employed to investigate the chemical compositions and states.

4.4. Electrochemical evaluation of HPI-Ti-2 inoculated with bacteria

The current-voltage (I–V) curves of HPI-Ti-2 were obtained using an electrochemical system mentioned in the electrochemical analysis. I–V curves were acquired with and without live/dead *E. coli*/*S. aureus*. For samples with bacteria on the surface, a bacterial solution with a concentration of 10^7 CFU mL^{-1} was applied to the sample surface and incubated at 37°C for 15 min to form a bacterial film. In contrast, dead bacteria were obtained by subjecting them to UV irradiation for 30 min before experimentation. Each experiment was repeated at least three times. Subsequently, electrochemical impedance spectra (EIS) of HPI-Ti-2 were also recorded in the presence or absence of live/dead *E. coli*/*S. aureus*. EIS measurements were conducted from 0.1 Hz to 100 kHz using a sinusoidal signal with an amplitude of 10 mV . The chemically discharging measurement was conducted by remaining HPI-Ti-2 inoculated with *S. aureus* in physiological saline without an external electrical source for certain times and then recharged.

4.5. Surface characterization

Contact angle measurement: The surface wettability of various samples was assessed using a contact angle instrument (Automatic Contact Angle Meter Model SL200B, Solon, China). Specifically, $2\text{ }\mu\text{L}$ of ultrapure water was dropped onto the sample surfaces, and images were captured with the integrated camera. Values of contact angles were obtained after analyzing the images with the built-in software.

Zeta potentials: The Zeta-potential results of various samples were determined using the Surpass electric measuring instrument (Anton Parr, Austria). In brief, two samples ($20\text{ mm} \times 10\text{ mm} \times 1\text{ mm}$) were fixed on a sample holder, and the sample gap was adjusted to $100 \pm 5\text{ }\mu\text{m}$. KCl solution (1 mM) was used as the testing medium, while NaOH (0.05 M) and HCl (0.05 M) were used to adjust the pH range.

Li ions release behavior: The HPI-Ti, HPI-Ti-1, and HPI-Ti-2 samples were immersed in a 0.9% NaCl solution (1 mL) at 37°C for 24 h. The released Li ions were measured using an inductively coupled plasma-atomic emission spectrometer (Varian Liberty 150, USA).

Protein adsorption: The samples were immersed in 1 mL bovine serum albumin (BSA, 1 mg mL⁻¹, Sigma Aldrich, USA) solution and incubated at 37 °C for 24 h. The total adsorbed BSA protein from different samples was determined and analyzed using the BCA Protein Assay Kit by measuring absorbance at 560 nm with an enzyme-labeled instrument (BioTek Cytation 5, USA).

Surface catalytic performance: The 3,3',5,5'-tetramethylbenzidine (TMB) colorimetric reaction is employed to detect oxidase activity in various samples. The detection principle involves the oxidation of colorless TMB solution to form a colored product. Each sample was placed in a 24-well plate and treated with 1 mL physiological saline solution containing TMB (2 mM). The absorbance values of the resulting TMB coloration were measured to determine the oxidase activity of different samples. After incubating each sample at 37 °C for 30 min, followed by cooling to room temperature, 100 µL of the mixture from each well was transferred to a 24-well plate. Subsequently, their absorbance within the range of 500 nm–800 nm was measured using an enzyme-labeled instrument.

4.6. In vitro antibacterial test

Escherichia coli (*E. coli*, ATCC 25922) and *Staphylococcus aureus* (*S. aureus*, ATCC 25923) were selected for antibacterial evaluation of various samples. Tryptic soy broth (TSB) and Luria–Bertani (LB) culture media were utilized to cultivate *S. aureus* and *E. coli*, respectively. For bacteria culture with various samples, 100 µL of bacterial suspension with a concentration of 10⁷ CFU mL⁻¹ was inoculated onto the sterilized sample surface and incubated at 37 °C for a specific time.

Antibacterial analysis: To evaluate the antibacterial efficacy, the plate count method was used. In detail, after culturing for 0, 0.5, 1, 2, 4, 6, and 24 h, bacteria from different samples were detached and collected. Subsequently, the collected bacteria suspensions were fold-diluted with saline solution, and 100 µL of diluted bacterial suspension was inoculated onto agar culture plates and incubated at 37 °C for 18 h. The resulting bacterial colonies were counted to determine the bacterial survival rates, calculated as antibacterial rate = $(N_C - N_S) / N_C \times 100\%$, where N_C represents the average number of bacteria in the control group (Ti) and N_S denotes the average number in the test groups (HPI-Ti, HPI-Ti-1, and HPI-Ti-2). Each group was replicated three times on agar culture plates, and results are presented as means ± standard deviation (SD).

Anti-biofilm tests: *S. aureus* was cultivated on various samples for 24 h and rinsed twice with a sterilized saline solution. In qualitative analysis, the Live/Dead BacLight Bacterial Viability Kit (Molecular Probes, USA) was used to stain the biofilm on each sample according to the manufacturer's instructions. Specifically, 400 µL of Live/Dead staining reagent was added and incubated at 37 °C for another 30 min. The samples were then visualized using a laser confocal fluorescence microscope (CLSM; TCS SP8, Germany). Besides, the samples with adhered bacteria were fixed and dehydrated before SEM observation.

In the quantitative analysis, the biofilm viability of *S. aureus* on different samples was assessed using the AlamarBlue assay (Thermo Fisher Scientific Inc., USA). Briefly, bacteria were seeded onto samples following standard bacterial culture protocols. After culturing for 24 h, the samples were cultured with 0.5 mL of sterilized saline containing 10 % alamarBlue and incubated for 1 h at 37 °C in darkness. Subsequently, 100 µL of the culture medium was transferred to a black 96-well plate, and fluorescence intensities were measured using an enzyme-labeled instrument (excitation wavelength: 560 nm; emission wavelength: 590 nm).

Bacteria morphology observation: To observe the bacteria morphology by SEM, bacteria on the samples were fixed with 2.5 % glutaraldehyde solution overnight, followed by dehydration using a gradient alcohol and hexamethyldisilazane solution. Subsequently, the bacteria morphologies were observed using SEM (S-3400N, HITACHI, Japan).

Agar diffusion assay and antimicrobial activity of extracts: The agar

diffusion assay was conducted to assess the antimicrobial activity of released ions from the samples. Briefly, 100 µL of *S. aureus* suspension with a concentration of 10⁷ CFU mL⁻¹ was introduced onto the agar plates. Subsequently, the samples were placed onto the agar plates and incubated for 24 h. Photographs of agar plates were taken. The width of inhibition zones surrounding the samples indicates the strength of antibacterial capabilities exhibited by released ions from sample surfaces. Additionally, the extraction solution from each sample was utilized to evaluate the antibacterial effects of released ions. In brief, immerse the sample in sterile physiological saline and incubate it at 37 °C in an incubator for the extraction of the sample. Bacteria with the final concentration of 10⁶ CFU mL⁻¹ were co-cultured with extract solution from each sample for 24 h, then 100 µL of bacterial suspension was introduced into the agar culture plates and cultured for another 18 h.

ROS level assessment: The intracellular ROS level was determined with 2',7'-dichlorodihydrofluorescein diacetate (DCFH-DA, Sigma, USA). Briefly, bacteria with a concentration of 10⁷ CFU mL⁻¹ were incubated with various samples for 6 h. Subsequently, 500 µL of 10 µM DCFH-DA solution was added and incubated for another 30 min at 37 °C. After vigorous shaking to separate the bacteria from the samples, the bacteria suspension from different samples was measured using a fluorophotometer (excitation wavelength: 485 nm, emission wavelength: 525 nm). The relative ROS level was then obtained by normalizing against the total number of bacteria reflected by DAPI staining.

Bacterial ATP level detection: According to the aforementioned cultivation method, *E. coli* and *S. aureus* were cultured on the samples for 6 h at 37 °C. The Enhanced ATP Assay Kit (Beyotime, China) was employed to evaluate the total intracellular ATP content. Following the kit instructions, extractions of bacterial ATP production were obtained, and fluorescence intensity was measured using an enzyme-labeled instrument. The ATP concentration was determined based on the standard curve provided in the kit for ATP samples. The total protein content from each group was assessed using the Pierce™ BCA Protein Assay Kit (Thermo Fisher Scientific, USA) with measurements performed at OD of 562 nm. To account for differences in bacterial numbers, ATP content was calculated using the formula: total ATP content = $C_{ATP} / C_{protein}$ where C_{ATP} represents tested ATP concentration and $C_{protein}$ corresponds to protein concentration.

Bacterial membrane potential analysis: The bacterial membrane potential was visualized by staining with 5-cyano-2,3-ditolyl tetrazolium chloride (CTC; Sigma, USA) reagent. During respiration of living bacteria, CTC is reduced to CTF (CTC formazan) via electron transport and forms a water-insoluble red fluorescent precipitate in the bacterial cytosol (excitation/emission wavelength: 488/620 nm). After incubating the bacteria on sample surfaces for 6 h, the sample was rinsed twice with PBS and then treated with 0.3 mM CTC solution (dissolved in 0.9 % NaCl) for another 1 h at 37 °C in darkness. DAPI was used to stain the nucleus of bacteria. Finally, bacterial membrane potential staining images were taken using a laser confocal fluorescence microscope (CLSM; TCS SP8, Germany).

4.7. In vitro biocompatibility evaluation

Cell culture: Gingival fibroblasts were identified as the predominant cell type in peri-implant soft tissue and played a crucial role in facilitating implant-tissue integration. To assess the biocompatibility of different samples, human gingival fibroblasts (HGFs; ScienCell Research Laboratories, USA) were employed. The HGFs were cultured with Fibroblast medium (FM, ScienCell Research Laboratories, USA) under a humidified atmosphere containing 5 % CO₂ at 37 °C. Cell passaging was performed every three days at a ratio of 1:3.

Cytoskeleton-staining: HGFs were seeded at a density of 5×10^4 cells per well onto samples in a 24-well plate. After incubation for 1, 4, and 24 h, the cells were fixed with 4 % paraformaldehyde (PFA, Sigma, USA) for 2 h at 4 °C in the dark. Subsequently, HGFs were permeabilized using

0.1 v/v % Triton X-100 solution for 2 min, followed by blocking Fc-receptors with the addition of 1 wt % BSA for 30 min. The cells were then stained with fluorescein isothiocyanate (FITC)-phalloidin (Sigma, USA) and DAPI sequentially for 60 min and 20 min, respectively. Finally, confocal laser scanning microscopy was employed to examine the cellular specimens.

Wound healing assay: The cell migration ability was assessed using a wound-healing assay. HGFs were seeded on the samples with a density of 5×10^4 cells mL^{-1} and allowed to reach confluence for 48 h. Subsequently, HGF monolayer “wounds” on the sample surfaces were created by scratching with a 0.2 mL plastic pipette tip. The cells were then cultured for another 6 h and 12 h in a fresh cell medium. Then, the samples were transferred to a new 24-well plate and fixed with 4 % PFA for 2 h at 4 °C. Subsequently, HGFs were stained with DAPI. Fluorescence images of the wounded regions on all the samples were acquired using CLSM.

Cell proliferation: HGFs were seeded with a density of 2×10^4 cells mL^{-1} onto various samples and cultured for 1, 3, and 5 days. At each time point, the culture medium was replaced with 0.5 mL of 10 % alamarBlue-containing full FM medium, and incubated at 37 °C for another 2 h. Subsequently, 100 μL of the culture medium mentioned above was transferred to a black 96-well plate for measurement using an enzyme-labeled instrument (excitation wavelength: 560 nm; emission wavelength: 590 nm).

Cell morphology: For cell morphology observation, HGFs were incubated on the samples for 1 day. Subsequently, the cells were rinsed twice with phosphate-buffered saline (PBS) and fixed in a 2.5 % glutaraldehyde solution at 4 °C for 2 h. The fixed cells were then dehydrated sequentially using ethanol solutions of increasing concentrations (30 %, 50 %, 75 %, 90 %, 95 %, and absolute ethanol) for 10 min each step. After dehydration, the samples underwent drying in a series of hexamethyl diethylamine/ethanol solutions with varying ratios (1:2, 1:1, 2:1, and pure hexamethyl diethylamine). SEM was employed to observe the cell morphologies on different sample surfaces. Before SEM examination, the platinum coating was applied to the HGF-containing samples to improve the conductivity.

Cell live/dead staining: The cytotoxicity of different samples was evaluated using a cell live/dead staining kit. HGFs with a cell density of 2×10^4 cells mL^{-1} were incubated with the samples for 4 days, followed by washing with PBS and transferring to a new culture plate. Subsequently, each sample was treated with 100 μL of calcein-AM and propidium iodide fluorescence dyes and incubated at 37 °C for 30 min. Finally, fluorescent images of the HGFs were captured using a fluorescent microscope.

Relative mRNA expression of HGFs adhesion-related genes: Real-time quantitative polymerase chain reaction (RT-qPCR) was used to detect the expression of adhesion-related genes in HGFs cultured on different groups of samples. Firstly, a 4 mL cell suspension with a cell density of 1.0×10^4 cells mL^{-1} was added to the 6-well cell culture plate. After incubation for 6 days, the culture medium was discarded, and the wells were washed twice with PBS. Then, each well was added with 1 mL TRIzol (Invitrogen, Thermo Fisher Scientific Inc., USA) for RNA extraction. The extracted RNA was transcribed into cDNA using a Roche cDNA reverse transcription kit (Roche, Switzerland). PCR experiments were conducted on a Roche LightCycler480 instrument using GAPDH as an internal reference gene. The relative expression levels of adhesion-related genes (FN, Talin 1, and Vinculin) were analyzed by the comparative quantification method known as $2^{-\Delta\Delta\text{Ct}}$ analysis. Gene primers were purchased from BioTNT (Shanghai), and triplicate samples were set up for each group along with two repeated experiments. The primer sequences used in this study are listed in [Table S4](#).

4.8. Animal experiments

Establishment of subcutaneous infection model: The animal surgical procedures were conducted in accordance with the Guidelines for Care

and Use of Laboratory Animals and approved by the Ethics Committee of Shanghai Xuhui District Dental Center (Protocol number: [2021]16). Male pathogen-free C57BL/6 mice, aged six weeks, were housed under specific pathogen-free conditions at the animal care facility in Shanghai JRDUN Biotech Co. Ltd. Initially, 20 μL of *S. aureus* (10^7 CFU mL^{-1}) was introduced, and incubated with various samples at 37 °C for 2 h to facilitate bacterial adherence on the samples. The mice were randomly divided into three groups: Ti, HPI-Ti, and HPI-Ti-1. Subsequently, they were anesthetized using a 1 wt% pentobarbital sodium solution (intraperitoneal injection; 10 μL g^{-1}). Thorough shaving of the skin overlying the surgical area was performed, and a 1-cm incision was made on their dorsal skin to create a subcutaneous pocket. One sample was placed into each mouse's pocket. The subcutaneous tissues and skin were then sutured, and the mice were fed for 1, 4, 7, or 14 days accordingly. At each designated time point, euthanasia was carried out by intraperitoneal injection of an overdose of anesthesia.

Antibacterial effects in vivo: The plate count method was employed to assess the efficacy of bacterial inactivation in different samples post-implantation. Initially, after implantation for 1 and 4 days, mice were euthanized, and the tissues in contact with the samples were collected. Subsequently, these tissues were immersed into 4 mL of sterile 0.9 % NaCl solution and then fold-diluted with saline solution. At last, 100 μL of the diluted solution was introduced onto agar plates and cultured for 18 h at 37 °C, then colony count was performed. Additionally, Giemsa and H&E staining of tissues surrounding the samples were also performed.

In vivo soft tissue compatibility tests: To assess the compatibility of various samples with soft tissues, mice were euthanized after 7 and 14 days of culturing. Subsequently, Hematoxylin & Eosin (H&E) staining was employed to evaluate the inflammatory response in the surrounding tissues, while Masson's trichrome staining was utilized to assess collagen deposition.

H&E staining for viscera of the mouse: To assess the biosafety of the different samples, various organs, including the heart, liver, spleen, lungs, and kidneys, were collected and subjected to histological examination using H&E staining.

4.9. Statistical analysis

The statistical analysis was performed using GraphPad Prism 9.5.1. Quantitative data are presented as mean \pm standard deviation (SD). Statistically significant differences (p) were assessed using a one-way analysis of variance (ANOVA) followed by Tukey's multiple comparison tests. A significance level of $p < 0.05$ was considered statistically significant and denoted by “*”, while $p < 0.01$ was represented by “**”, $p < 0.001$ was indicated as “***”, and $p < 0.0001$ was indicated as “****”.

Data availability

All data associated with this study are present in the paper or the supplemental information. Raw data are available upon request.

Ethics approval and consent to participate

The animal surgical procedures were conducted in accordance with the Guidelines for Care and Use of Laboratory Animals and approved by the Ethics Committee of Shanghai Xuhui District Dental Center (Protocol number: [2021]16).

CRediT authorship contribution statement

Fang Wang: Writing – review & editing, Writing – original draft, Methodology, Formal analysis, Data curation, Conceptualization. **Shiwei Guan:** Writing – review & editing, Methodology, Investigation, Conceptualization. **Min Xing:** Methodology, Investigation. **Wenhao Qian:** Methodology, Investigation. **Jiajun Qiu:** Writing – review &

editing, Methodology, Investigation, Funding acquisition, Formal analysis. **Xuanyong Liu:** Writing – review & editing, Funding acquisition, Conceptualization.

Declaration of competing interest

Xuanyong Liu is an editorial board member for *Bioactive Materials* and was not involved in the editorial review or the decision to publish this article. All authors declare that there are no competing interests.

Acknowledgments

This work was financially supported by National Natural Science Foundation of China (52272283), Key Research and Development Program of Zhejiang Province (2023C03G9103957), Young Elite Scientists Sponsorship Program by CAST (YESS) (2022-2024QNRC001), Youth Innovation Promotion Association CAS (2023263), Major/Key Program of State Key Laboratory for Modification of Chemical Fibers and Polymer Materials (23M1060280).

Appendix A. Supplementary data

Supplementary data to this article can be found online at <https://doi.org/10.1016/j.bioactmat.2024.05.029>.

References

- A.F. Vonrecum, Applications and failure modes of percutaneous devices - a review, *J. Biomed. Mater. Res.* 18 (1984) 323–336.
- J. Leng, Y. He, Z. Yuan, B. Tao, K. Li, C. Lin, K. Xu, M. Chen, L. Dai, X. Li, T. J. Huang, K. Cai, Enzymatically-degradable hydrogel coatings on titanium for bacterial infection inhibition and enhanced soft tissue compatibility via a self-adaptive strategy, *Bioact. Mater.* 6 (2021) 4670–4685.
- T. Ding, L. Zhang, J. Han, J. Zhou, Y. Han, Photo-responded antibacterial therapy of reinfection in percutaneous implants by nanostructured bio-heterojunction, *Small* 19 (2023) 06265.
- T. Weigel, B. Christ, S. Dembski, A. Ewald, D. Groneberg, J. Hansmann, R. Luxenhofer, M. Metzger, H. Walles, C. Willy, F. Groeber-Becker, J. Probst, Biomimetic connection of transcutaneous implants with skin, *Adv. Healthcare Mater.* 12 (2023) 01131.
- M.N. Abdallah, Z. Badran, O. Ciobanu, N. Hamdan, F. Tamimi, Strategies for optimizing the soft tissue seal around osseointegrated implants, *Adv. Healthcare Mater.* 6 (2017) 1700549.
- V.T.H. Pham, T. Vi Khanh, A. Orlowska, S. Ghanaati, M. Barbeck, P. Booms, A. Fulcher, C.M. Bhadra, R. Buividas, V. Baulin, C.J. Kirkpatrick, P. Doran, D. E. Mainwaring, S. Juodkazis, R.J. Crawford, E.P. Ivanova, "Race for the surface": eukaryotic cells can win, *ACS Appl. Mater. Interfaces* 8 (2016) 22025–22031.
- J.W. Costerton, P.S. Stewart, E.P. Greenberg, Bacterial biofilms: a common cause of persistent infections, *Science* 284 (1999) 1318–1322.
- H. Chouirfa, H. Bouloussa, V. Mignonney, C. Falentin-Daudre, Review of titanium surface modification techniques and coatings for antibacterial applications, *Acta Biomater.* 83 (2019) 37–54.
- W. Li, E.S. Thian, M. Wang, Z. Wang, L. Ren, Surface design for antibacterial materials: from fundamentals to advanced strategies, *Adv. Sci.* 8 (2021) 2100368.
- Z. Cui, J. Zhu, H. Jiang, S. Wu, S. Zhu, Research progress of the surface modification of titanium and titanium alloys for biomedical application, *Acta Metall. Sin.* 58 (2022) 837–856.
- M.-L. Jourdain, F. Velard, L. Pierrard, J. Sergheraert, S.C. Gangloff, J. Braux, Cationic antimicrobial peptides and periodontal physiopathology: a systematic review, *J. Periodontol. Res.* 54 (2019) 589–600.
- A. Wang, S. Duan, X. Ding, N. Zhao, Y. Hu, X. Ding, F.-J. Xu, Bioswitchable antibacterial coatings enable self-sterilization of implantable healthcare dressings, *Adv. Funct. Mater.* 31 (2021) 2011165.
- F. Yang, D. Huo, J. Zhang, T. Lin, J. Zhang, S. Tan, L. Yang, Fabrication of graphene oxide/copper synergistic antibacterial coating for medical titanium substrate, *J. Colloid Interface Sci.* 638 (2023) 1–13.
- T. Guo, K. Gulati, H. Arora, P. Han, B. Fournier, S. Ivanovski, Orchestrating soft tissue integration at the transmucosal region of titanium implants, *Acta Biomater.* 124 (2021) 33–49.
- G.E. Salvi, D.D. Bosshardt, N.P. Lang, I. Abrahamsson, T. Berglundh, J. Lindhe, S. Ivanovski, N. Donos, Temporal sequence of hard and soft tissue healing around titanium dental implants, *Periodontol.* 68 (2015) (2000) 135–152.
- H. Yao, L. Jiang, X. Luo, D. Zou, L. Liu, P. Yang, J. Chen, A. Zhao, N. Huang, Highly efficient photocatalytic anti-bacterial Ag doped titanium dioxide nanofilms with combination of reactive oxygen species and Ag ions releasing for application of vascular implants, *Adv. Mater. Interfac.* 8 (2021) 2100892.
- K.E. Dineley, T.V. Votyakova, I.J. Reynolds, Zinc inhibition of cellular energy production: implications for mitochondria and neurodegeneration, *J. Neurochem.* 85 (2003) 563–570.
- X. Zhi, H. Fang, C. Bao, G. Shen, J. Zhang, K. Wang, S. Guo, T. Wan, D. Cui, The immunotoxicity of graphene oxides and the effect of PVP-coating, *Biomaterials* 34 (2013) 5254–5261.
- P. Mitchell, Coupling of phosphorylation to electron and hydrogen transfer by a chemi-osmotic type of mechanism, *Nature* 191 (1961) 144–148.
- R. Guo, S. Zong, M. Wu, J. Gu, M. Yang, Architecture of human mitochondrial respiratory megacomplex I2III2IV2, *Cell* 170 (2017) 1247–1257.
- M. Sarewicz, A. Osyczka, Electronic connection between the Quinone and Cytochrome c redox pools and its role in regulation of mitochondrial electron transport and redox signaling, *Physiol. Rev.* 95 (2015) 219–243.
- C. Liu, Z. Guo, H. Zhang, J. Li, C. Zhu, G. Zhu, Single-cell Raman spectra reveals the cytochrome c-mediated electron transfer in nanoscale zero-valent iron coupled denitrification process, *Chem. Eng. J.* 454 (2023) 140241.
- B.E. Logan, Exoelectrogenic bacteria that power microbial fuel cells, *Nat. Rev. Microbiol.* 7 (2009) 375–381.
- G. Wang, K. Tang, W. Jiang, Q. Liao, Y. Li, P. Liu, Y. Wu, M. Liu, H. Wang, B. Li, J. Du, P.K. Chu, Quantifiable relationship between antibacterial efficacy and electro-mechanical intervention on nanowire arrays, *Adv. Mater.* 35 (2023) 12315.
- G. Wang, K. Tang, Z. Meng, P. Liu, S. Mo, B. Mehrjou, H. Wang, X. Liu, Z. Wu, P. K. Chu, A quantitative bacteria monitoring and killing platform based on electron transfer from bacteria to a semiconductor, *Adv. Mater.* 32 (2020) 2003616.
- D.H. Wang, J. Tan, H.Q. Zhu, Y.F. Mei, X.Y. Liu, Biomedical implants with charge-transfer monitoring and regulating abilities, *Adv. Sci.* 8 (2021) 2004393.
- H. Strahl, L.W. Hamoen, Membrane potential is important for bacterial cell division, *Proc. Natl. Acad. Sci. U.S.A.* 107 (2010) 12281–12286.
- R. Shi, J. Zhang, J. Tian, C. Zhao, Z. Li, Y. Zhang, Y. Li, C. Wu, W. Tian, Z. Li, An effective self-powered strategy to endow titanium implant surface with associated activity of anti-biofilm and osteogenesis, *Nano Energy* 77 (2020) 105201.
- G. Wang, H. Feng, L. Hu, W. Jin, Q. Hao, A. Gao, X. Peng, W. Li, K.-Y. Wong, H. Wang, Z. Li, P.K. Chu, An antibacterial platform based on capacitive carbon-doped TiO₂ nanotubes after direct or alternating current charging, *Nat. Commun.* 9 (2018) 2055.
- M. Zhao, B. Song, J. Pu, T. Wada, B. Reid, G. Tai, F. Wang, A. Guo, P. Walczysko, Y. Gu, T. Sasaki, A. Suzuki, J.V. Forrester, H.R. Bourne, P.N. Devreotes, C. D. McCaig, J.M. Penninger, Electrical signals control wound healing through phosphatidylinositol-3-OH kinase-gamma and PTEN, *Nature* 442 (2006) 457–460.
- M. Zhao, Electrical fields in wound healing—An overriding signal that directs cell migration, *Semin. Cell Dev. Biol.* 20 (2009) 674–682.
- C.D. McCaig, A.M. Rajnicek, B. Song, M. Zhao, Controlling cell behavior electrically: current views and future potential, *Physiol. Rev.* 85 (2005) 943–978.
- P. Sharma, D. Damien, K. Nagarajan, M.M. Shaijumon, M. Hariharan, Perylene-polyimide-Based organic electrode materials for rechargeable lithium batteries, *J. Phys. Chem. Lett.* 4 (2013) 3192–3197.
- Y. Zhao, S. Zhang, S. Xu, X. Li, Y. Zhang, Y. Xu, J. Zhou, H. Bi, F. Huang, T. Lin, A pi-conjugated polyimide-based high-performance aqueous potassium-ion asymmetric supercapacitor, *Macromol. Rapid Commun.* 43 (2022) 2200040.
- G. Dawut, Y. Lu, Q. Zhao, J. Liang, Z.-L. Tao, J. Chen, Quinones as electrode materials for rechargeable lithium batteries, *Acta Phys. Chim. Sin.* 32 (2016) 1593–1603.
- J. Huang, P. Yu, M. Liao, X. Dong, J. Xu, J. Ming, D. Bin, Y. Wang, F. Zhang, Y. Xia, A self-charging salt water battery for antitumor therapy, *Sci. Adv.* 9 (2023) eadf3992-eadf3992.
- X. Dong, L. Chen, J. Liu, S. Haller, Y. Wang, Y. Xia, Environmentally-friendly aqueous Li (or Na)-ion battery with fast electrode kinetics and super-long life, *Sci. Adv.* 2 (2016) e1501038.
- B.E. Conway, Transition from "supercapacitor" to "battery" behavior in electrochemical energy storage, *J. Electrochem. Soc.* 138 (1991) 1539–1548.
- Q. Jiang, H. Sun, D. Zhao, F. Zhang, D. Hu, F. Jiao, L. Qin, V. Linseis, S. Fabiano, X. Crispin, Y. Ma, Y. Cao, High thermoelectric performance in n-type perylene bisimide induced by the soot effect, *Adv. Mater.* 32 (2020) 2002752.
- L. Chen, W. Li, Z. Guo, Y. Wang, C. Wang, Y. Che, Y. Xia, Aqueous lithium-ion batteries using O-2 self-elimination polyimides electrodes, *J. Electrochem. Soc.* 162 (2015) A1972–A1977.
- F. Goetz, S. Mayer, Both terminal oxidases contribute to fitness and virulence during organ-specific *Staphylococcus aureus* colonization, *mBio* 4 (2013) e00976, 13.
- Q. Yan, L. Chang Ming, B. Shu-Juan, L. Zhisong, H. Yunhan, Direct electrochemistry and electrocatalytic mechanism of evolved *Escherichia coli* cells in microbial fuel cells, *Chem. Commun.* (2008) 1290–1292.
- T.J. Silhavy, D. Kahne, S. Walker, The bacterial cell envelope, *Cold Spring Harbor Perspect. Biol.* 2 (2010) a000414.
- M.E. Hernandez, D.K. Newman, Extracellular electron transfer, *Cell. Mol. Life Sci.* 58 (2001) 1562–1571.
- R.-Z. Zhao, S. Jiang, L. Zhang, Z.-B. Yu, Mitochondrial electron transport chain, ROS generation and uncoupling (Review), *Int. J. Mol. Med.* 44 (2019) 3–15.
- A.J. Zollinger, M.L. Smith, Fibronectin, the extracellular glue, *Matrix Biol.* 60–61 (2017) 27–37.
- M. Das, S.S. Ithychanda, J. Qin, E.F. Plow, Mechanisms of talin-dependent integrin signaling and crosstalk, *Biochim. Biophys. Acta Biomembr.* 1838 (2014) 579–588.
- R. Boujema-Paterski, B. Martins, M. Eibauer, C.T. Beales, B. Geiger, O. Medalia, Talin-activated vinculin interacts with branched actin networks to initiate bundles, *Elife* 9 (2020) e53990.